Chemical Geology 662 (2024) 122253

Contents lists available at ScienceDirect

Chemical Geology

journal homepage: www.elsevier.com/locate/chemgeo

Weathering-induced Sb isotope fractionation during leaching of stibnite and formation of secondary Sb minerals

Andreas B. Kaufmann [a,b,*], Marina Lazarov [b], Ingo Horn [b], Martin Števko [c,d], Tamara Đorđević [e,f], Stefan Kiefer [a], Stefan Weyer [b], Juraj Majzlan [a]

[a] Institute of Geosciences, Friedrich Schiller University Jena, Jena, Germany
[b] Institute of Earth System Sciences, Leibniz University Hannover, Hannover, Germany
[c] Earth Science Institute v.v.i., Slovak Academy of Sciences, Dúbravská cesta 9, P. O. BOX 106, 840 05 Bratislava, Slovakia
[d] Department of Mineralogy and Petrology, National Museum, Cirkusová 1740, 193 00 Praha 9, Horní Počernice, Czech Republic
[e] E057-02 USTEM, Vienna University of Technology, Stadionallee 2, 1020 Wien, Austria
[f] Institut für Mineralogie und Kristallographie, Universität Wien, Josef-Holaubek-Platz 2, 1090 Wien, Austria

ARTICLE INFO

Editor: Oleg Pokrovsky

Keywords:
Sb isotopes
Fractionation
Oxidative leaching
Stibnite
Weathering
Secondary minerals

ABSTRACT

In this work, we investigated the extent of antimony (Sb) isotopic fractionation during weathering of stibnite at supergene conditions. Antimony isotope data have been obtained from secondary Sb minerals collected from Pezinok, Dobšiná (both Slovakia) and Allchar (North Macedonia) deposits and mine tailings. The Sb isotope compositions of sulfides and secondary Sb minerals formed on the primary stibnite [Sb_2S_3] or in mine tailings grains were compared with each other. Furthermore, we experimentally investigated Sb isotope fractionation during stibnite leaching with different acids. Our study reveals a large isotopic range for $\delta^{123}Sb$ (from −0.50 to +0.69 ‰) for secondary Sb minerals. They are either isotopically indistinguishable or isotopically lighter than the primary stibnite. Isotopically indistinguishable weathering products likely formed by quantitative Sb transfer from stibnite to the secondary minerals, such as brandholzite [$Mg(H_2O)_6[Sb(OH)_6]_2$] from Pezinok. Isotopic fractionation towards lighter $\delta^{123}Sb$ was observed for adsorption of Sb onto iron oxides. Distinctly isotopically lighter $\delta^{123}Sb$ was observed in secondary Sb minerals tripuhyite [$FeSbO_4$], chapmanite [$Fe^{3+}_2Sb^{3+}(Si_2O_5)O_3(OH)$], hydroxyferroromeite [$Fe_2Sb_2O_6(OH)$], and stibiconite [$Sb_3O_6OH$] that either replace stibnite or formed in mine tailings from the pore solutions. These secondary minerals were likely generated by partial precipitation of Sb from aqueous solutions produced by dissolution of stibnite. In the leaching experiments with HCl and oxalic acid, Sb was leached without significant isotope effects during the first 2–3 days, followed by a drop of the dissolved Sb concentration associated with Sb isotope fractionation towards high $\delta^{123}Sb$ in the leachate (by up to 0.5 ‰) after 4–7 days. We interpret these observations to be related to the precipitation of secondary Sb oxides with low $\delta^{123}Sb$, resulting in an isotopically heavy dissolved Sb pool. These findings are in agreement with previous results of isotopically heavy groundwater and mine drainage water with $\delta^{123}Sb > +0.36$ ‰ that may suggest that the 'truly' dissolved (operationally defined as <0.45 μm) Sb fraction in general may be isotopically heavy.

1. Introduction

Natural weathering and human activities during the extraction of raw materials lead to release and deposition of metals and metalloids into soils, sediments, and aquatic environments (Akcil and Koldas, 2006; Lottermoser, 2010; Simate and Ndlovu, 2014; Lindsay et al., 2015; Masindi and Muedi, 2018). Of the metalloids, antimony (Sb) is of environmental concern due to its perceived toxicity (Cooper and Harrison, 2009; Guo et al., 2016), causing risk to human health and ecosystems (Herath et al., 2017; He et al., 2019). Near the actively exploited mines in China, Sb reached up to 11,800 μg kg^{-1} in soils (Okkenhaug et al., 2011) and 13,350 μg L^{-1} in rivers (Li et al., 2019). These values are several orders of magnitude higher than those in uncontaminated soils (~1 μg g^{-1}; Tschan et al., 2009) or the threshold Sb concentration in drinking water defined by the World Health Organization (20 μg L^{-1}; WHO, 2022). The toxicity and mobility of Sb depend

* Corresponding author at: Institute of Geosciences, Friedrich Schiller University Jena, Jena, Germany.
E-mail address: a.kaufmann@mineralogie.uni-hannover.de (A.B. Kaufmann).

https://doi.org/10.1016/j.chemgeo.2024.122253
Received 21 March 2024; Received in revised form 20 June 2024; Accepted 24 June 2024
Available online 25 June 2024
0009-2541/© 2024 The Authors. Published by Elsevier B.V. This is an open access article under the CC BY license (http://creativecommons.org/licenses/by/4.0/).

strongly on its chemical and redox speciation. In nature, Sb occurs dominantly as Sb^{5+} or Sb^{3+}; of which Sb^{3+} is assumed to be more toxic but less mobile than Sb^{5+} (Filella et al., 2002; Wilson et al., 2010; Herath et al., 2017). Investigations of mine tailings of Sb deposits show that immobilization of Sb is mainly controlled by adsorption to Fe oxides and clays (Wilson and Webster-Brown, 2009; Bolanz et al., 2013). Adsorption, remineralization (Burton et al., 2020) of Sb^{5+} on Fe oxides, and formation of tripuhyite [$FeSbO_4$] and schafarzikite [$FeSb_2O_4$] have been suggested by Leverett et al. (2012) as the ultimate sink of Sb in the environment.

Stable isotopes of metals and metalloids are frequently applied in environmental studies as tracers of the source and processes of pollution (e.g., Wiederhold, 2015). Some isotopic systems, such as Cu, Zn, and Fe, were extensively discussed and summarized by Moynier et al. (2017), Dauphas et al. (2017), and Johnson et al. (2020). However, only a few studies dealt with Sb isotopic variations in near-surface environments (Resongles et al., 2015; Liao et al., 2023; Wen et al., 2023; Guillevic et al., 2024; Liu et al., 2024; Wu et al., 2024). Antimony has two stable sotopes with masses of ^{121}Sb and ^{123}Sb with roughly equal abundances (Meija et al., 2016). Rouxel et al. (2003) and Zhai et al. (2021) showed an isotopic variation of around ~2 ‰ for hydrothermal systems. Smaller isotopic variations (~1 ‰) were observed by Resongles et al. (2015) and Wen et al. (2023) for river water that was affected by mining. Soils and sediments close to mining regions appear to be enriched in the heavy Sb isotope, with no obvious isotope fractionation between sediment and river water during adsorption of Sb to Al—Fe oxides in the sediment (Guillevic et al., 2024; Liu et al., 2024). Experimental studies (Rouxel et al., 2003; MacKinney, 2016; Veldhuizen et al., 2023) found isotope fractionation of up to 1.4 ‰ during abiotic reduction of Sb^{5+} to Sb^{3+}. Other experimental studies devoted to adsorption processes showed a strong dependence of Sb isotopic fractionation on adsorption agents. Zhou et al. (2022) reported that there is no Sb isotope fractionation during adsorption onto aluminum oxides. Conversely, adsorption onto Fe oxides (Luo et al., 2023; Zhou et al., 2023; Ferrari et al., 2024), clays (kaolinite and montmorillonite), and Mn oxides (Wu et al., 2024) caused isotopic fractionation of up to 2.35 ‰. Ab initio calculations (Ferrari et al., 2022) suggested that the oxidative dissolution of stibnite (Sb_2S_3) should lead to an enrichment of the heavier Sb isotopes in secondary Sb oxides with more oxidized Sb species. The Sb release from stibnite depends strongly on pH (Biver and Shotyk, 2012), light irradiation (Hu et al., 2015), dissolved O_2 (Leuz and Johnson, 2005), presence of ions (Ca^{2+}, Mg^{2+}; Biver and Shotyk (2012); Fe^{3+}, Cl^- and As^{3+}; Asta et al., 2012), and biological activity (Loni et al., 2020). All these factors may additionally contribute to isotopic fractionation and the direction and magnitude of this fractionation is unknown at this time.

In this study, we report the Sb isotopic composition of a variety of secondary Sb minerals produced by weathering of stibnite. These minerals provide examples of stibnite in situ weathering and replacement or an intermediate step via the transport of Sb in aqueous solutions. The mineralogy of the sampling areas was documented in detail previously (Pršek et al., 2009; Majzlan et al., 2011; Lalinská-Voleková et al., 2012; Majzlan et al., 2016; Đorđević et al., 2021a and references therein). A comprehensive description of the various secondary Sb oxides in different weathering environments is given by Roper et al. (2012) and Majzlan (2021). The measured isotopic composition of the secondary minerals was compared with that of the precursor stibnite from each studied site. Particular attention was paid to the relationship between the nature (i.e., changes in mineral and chemical composition) of the weathering process, the textural features of the secondary minerals, and their Sb isotopic signature. The observations in the field settings are supported by laboratory stibnite leaching experiments with various acids for which Sb concentrations and isotopic compositions of the released Sb were determined. The results of this work can be used to develop Sb isotopic composition as a tracer for a better understanding of weathering processes of Sb deposits. It also provides hints regarding the effect of stibnite weathering on the Sb isotope composition of surface water, groundwater, and oceans.

2. Description of the study areas

2.1. Pezinok (Malé Karpaty Mts., Western Carpathians, Slovakia)

The deposit Pezinok is located in the Malé Karpaty Mts., the westernmost mountain range of the Western Carpathians in Slovakia. GPS coordinates of the large tailing pond, the source of most samples used in this work, are 48.31884° N and 17.23756° E. Samples of chapmanite [$Fe_2^{3+}Sb^{3+}(Si_2O_5)O_3(OH)$] used in this work come from the historical finds described by Polák (1983) from the Sirková adit of the Pezinok deposit (adit entrance at 48.31500° N, 17.23972° E).

The ore mineralization is hosted by quartz-carbonate (ferroan dolomite) lenses, veinlets, and impregnations in regionally metamorphic rocks (Cambel and Khun, 1983) that were formed from a Devonian volcano-sedimentary complex. The mineralization is bound to carbonaceous metasilicites (metamorphosed black shales) embedded in actinolite schists and amphibolites (Chovan et al., 1992; Chovan et al., 1994). This work focuses on stibnite that was the dominant ore mineral in the strata-bound Sb-Au-As mineralization (Chovan et al., 1994). A detailed mineralogical and Sb isotope composition analysis on primary minerals of this mineralization was performed by Kaufmann et al. (2023).

Mining activities near Pezinok date back to the late 17th century with the most prolific period in 1940's. Between 1790 and the end of mining activity in 1992, the deposit produced 15,000 tons of antimony. Since 1906, the ores were extracted by froth flotation, after grinding to a particle size of 40–90 μm and extraction in aqueous media with a pH value between 6.5 and 8.0. Extraction by flotation was technologically very difficult, therefore, a significant fraction of Sb sulfides (75% of stibnite) and most Sb oxides were not recovered and escaped into the waste (Grexová, 1991). For this reason, a large and a small impoundment hold around ~380,000 m^3 of mining waste, containing ~6000 t of Sb (Majzlan et al., 2011). The pH in the tailings is buffered by abundant carbonates, which represent 3.9 wt% of the impoundment material, causing neutral mine drainage. Majzlan et al. (2011) estimated that the tailings contain on average 6.6 ± 3.0 (1σ) g Sb/kg and X-ray diffraction patterns revealed that the tailing is dominated by quartz, plagioclase, actinolite, illite, calcite, dolomite, and pyrite. Although much stibnite escaped into the waste, Lalinská-Voleková et al. (2012) found no stibnite in the oxidized zone of the tailings today, likely due to rapid weathering of this mineral.

The occurrence of chapmanite at Pezinok was described by Polák (1983). Chapmanite was found in fractures of dark quartz, together with siderite and minute pyrite crystals. We used samples collected in 1980's during the mine operation. Abundant pyrite created acid mine drainage conditions that destroyed the occurrence completely.

2.2. Dobšiná (Spišsko-gemerské Rudohorie Mts., Western Carpathians, Slovakia)

The deposit Dobšiná is located in eastern Slovakia. One of the small sites, called Hlboká dolka (Tiefengründl-Steingeräusch) was mined historically for stibnite and is located at 48.80338° N, 20.38265° E. Stibnite was the main ore mineral, accompanied by chalcostibite [$CuSbS_2$] and tetrahedrite [$(Cu,Fe)_{12}Sb_4S_{13}$]. All of them are hosted by hydrothermal quartz-carbonate (ferroan dolomite) veins in metamorphosed acidic volcanic rocks. The samples used in this work were found on the dumps of the deposit and their spatial relationship to other minerals and structural position are not known. Mining commenced in 1690 (Koděra et al., 1986), the ores were hand-picked and the unwanted material was deposited on the dumps. It can be assumed that the samples collected were exposed to the atmosphere for at least 100 years.

2.3. Allchar (Kožuf Mountains, North Macedonia)

The abandoned Sb-As-Tl-Au Allchar mine is located in the south of North Macedonia near the hamlet of Majdan at the north-western margins of the Kožuf Mountains. Compared to global thallium accumulations, the Allchar deposit has remarkably high thallium grades (500 tons). In addition to having high concentrations of As (in realgar and orpiment) and Sb (in stibnite), the Allchar deposit is the first Carlin-type gold deposit discovered in the Balkan Peninsula in the mid-1980s (Percival and Radtke, 1994; Volkov et al., 2006; Boev et al., 2012; Strmić et al., 2018). Since the 15th century, the deposit has been a source of As. Later, with sporadic breaks, it also served as a source of Sb (1881–1973).

The host rocks are dominated by Triassic dolomites, covered by a Tertiary volcano-sedimentary sequence of tuffs and dolomites. The mineralization of Allchar is closely associated with a Pliocene volcanic complex (altered latite, dacite, and andesite) (Janković, 1993; Percival and Radtke, 1994; Pavićević et al., 2006). Three loosely defined zones contain the mineralization at Allchar (Janković and Jelenković, 1994): (i) the high-temperature, southern zone; (ii) the central zone, which is dominated by Sb and Au and contains As, Tl, minor Ba, Hg, and traces of Pb; and (iii) the northern zone, which is dominated by As—Tl mineralization and contains minor Sb, Hg, and trace amounts of Au.

The primary minerals found in the deposit are pyrite, marcasite, stibnite, realgar, and orpiment; these minerals are hosted by a fine-grained quartz or dolomite gangue. With the exception of the Crven Dol locality in the northern part of the deposit (Đorđević et al., 2021a), the pronounced secondary phase assemblages are far from being fully investigated. Among secondary phases identified, iron and calcium arsenates, iron oxides, and Fe—Sb oxides, both amorphous and crystalline are the most widespread.

3. Materials and methods

3.1. Mineral characterization

The samples from the Pezinok deposit were collected in the abandoned mines and from the tailing impoundments as described by Majzlan et al. (2011). From the large tailing impoundment, the sand-silty material and the underlying alluvial sediments were sampled in a borehole PK-6 with a length of 20 m (Majzlan et al., 2011). The recovered and sealed material in plastic bags was stored in a refrigerator. To enrich the samples with the heavy fractions, samples were treated with panning in water or ethanol. The heavy-mineral concentrates from Pezinok were prepared as thin sections. In contrast, the samples from the Dobšiná deposit were picked from the loose material on the surface of the sampled historical dump. All thin and polished sections of the weathering products (excluding chapmanite) were studied in reflected polarized light. The sheet silicate chapmanite formed greenish-yellow crusts that were not amenable to embedding and polishing necessary for microscopy and LA-MC-ICP-MS measurements. Chapmanite was separated from the associated minerals by the same protocol for clay minerals as in Majzlan et al. (2021).

The Allchar sample used in this work was collected from a mining waste dump in the central part of the deposit (GPS coordinates 41°08′54.2″ N, 21°57′29.3″ E). Approximately 25 kg sample was dug out, sieved using 1 cm-mesh stainless-steel sieve, packed, and carried to the nearby creek in order to separate the heavy minerals by panning. In the laboratory, the dry, panned sample was sieved to the ≤2-mm fraction and homogenized. The heavy fraction was further concentrated using sodium metatungstate solution (specific gravity 2.80 $g \cdot cm^{-3}$). Both heavy-grain concentrates and the ≤2 mm fraction were prepared as standard polished sections for subsequent scanning electron microscopy (SEM) with energy-dispersive X-ray spectroscopy (EDX) and electron microprobe analysis (EMPA). These samples were already described by Đorđević et al. (2021b). They are composed mostly of dolomite, quartz, gypsum, pyrite, marcasite, stibnite, realgar and baryte, followed by muscovite, kaolinite-group minerals and various metal-Sb-oxides. The Tl sulfosalts fangite, lorándite and pierrotite are the primary Tl-minerals. Secondary mineral assemblage is characterized by jarosite-group minerals, scorodite, hydroxyferroroméite, and hydroxycalcioroméite.

Quantitative chemical analyses of the major and minor elements of most of the minerals from the Pezinok and Dobšiná deposits studied were carried out with a JEOL JXA-8230 electron microprobe coupled with wavelength-dispersive X-ray spectrometers at the University of Jena (Germany). Chemical composition of the investigated minerals from Allchar was obtained with a field-emission electron microprobe (FE-EMPA) JEOL JXA 8530-F, equipped with five wavelength-dispersive spectrometers (WDS) and two energy-dispersive spectrometers (EDS) in Vienna (Austria). For both operative conditions were 15 kV acceleration voltage, 20 nA beam current, and 5 μm beam size (Jena) and a fully focused beam (Vienna). For quantification, a ZAF correction was applied and the content was calculated in oxides. The counting times were 20 s on peak and 20 s on the background points. Standard materials with lines and detection limits for the analyses are presented in wt% as follows (Jena; Vienna): Sb (Lα, Sb_2S_3, 0.08; 0.06), S (Kα, $BaSO_4$, 0.04; troilite, FeS, 0.02), Fe (Kα, Fe_2O_3, 0.05; troilite, FeS, 0.04), Pb (Mα, PbS, 0.09; − = not measured in Vienna), As (Kα, FeAsS, 0.05; Lα, $TlAsS_2$, 0.07), Cu (Kα, $CuFeS_2$, 0.05; −), Ni (Kα, Ni metal, 0.04; −), Al (Kα, Al_2O_3, 0.04; −), Si (Kα, $CaSiO_3$, 0.07; Marjalahti olivine $(Mg,Fe)_2SiO_4$, 0.03), Ca (Kα, apatite, 0.05; Kα, wollastonite $CaSiO_3$, 0.04). The detection limits for elements only measured in Vienna are Mn (Kα, tephroite Mn_2SiO_4, 0.03), and Tl (Mα, $TlAsS_2$, 0.07). Overlap corrections were performed on the interference from As Lα on Sb Lβ1.

Selected samples were analyzed by powder X-ray diffraction (PXRD) and Raman spectroscopy. The PXRD analyses were performed with a Bruker D8 Advance DaVinci diffractometer at room temperature using CuKα radiation (Jena). The patterns were collected in the angular range of 5–90°2θ with a step size of 0.01°2θ and a dwell time of 1 s per step. Raman spectra were obtained using a Horiba LabRam-HR system equipped with an Olympus BX41 optical microscope in the spectral range between 100 and 1200 cm^{-1} (532 nm He—Ne laser; laser power was controlled by means of a series of density filters; Objective 50×; N. A. = 0.90) (Vienna). The system was calibrated before each experimental session using the 520.6 cm^{-1} Raman band of silicon. The spectra were collected using multiple acquisitions and with single counting time of 150 s. Backscattered radiation was analyzed with an 1800 mm^{-1} grating monochromator. Spectral manipulation such as smoothing and normalization were performed using the Labspec 5 software package. All Raman studies were performed on the polished sections at the Fb–Sb–O grain depicted in the Fig. 2e.

3.2. Leaching experiment

For the batch leaching experiment, we selected a stibnite sample from the Dúbrava Sb—Au deposit, described and analyzed in detail previously by Kaufmann et al. (2021). For the purposes of this study, the sample was crushed and ground in an agate mortar into fine powder. The electric conductivity and oxidation-reduction potential (SenTix ORP-T 900(—P) + Xylem pH/Cond 3320), and pH value (Mettler-Toledo FG2) were measured at ambient room conditions only during the start and end of the experiment from a separated leachate aliquot. This was required to reduce the risk of contamination of our leachate for isotope and concentration measurements and to spare aliquots for the prolong duration of the experiments. No buffer was used; instead, the pH value was allowed to drift over the duration of the leaching experiments.

The leaching experiment was performed at room temperature. Aliquots of the sample were brought in contact with different acids and kept in these acids for the duration of the experiment. In order to minimize contamination by the chemicals used for digestion, only distilled acids were used throughout these experiments.

In the leaching experiment, 0.14 g of stibnite powder was added into each of three pre-cleaned (with MQ water) 50 mL centrifuge tubes. Each of the three tubes was filled with 22 mL of a different acid, namely (1) 0.5 M HNO_3, (2) 0.05 M HCl, or (3) 0.1 M oxalic acid. The lids were screwed on to reduce oxygen access and centrifuge tubes were placed on a shaker table for 168 h. The time frame of 168 h was chosen because the experiment by Biver and Shotyk (2012) already showed total dissolved antimony concentrations in the leachate reached a stationary state after 24–36 h of leaching. The variety of acids was selected because a previous study (Fernandez and Borrok, 2009) showed that HCl and HNO_3 could cause in a different isotopic evolution during leaching. Oxalic acid was selected because it is a ubiquitous organic acid that plays an important role during mineral weathering processes. At pre-selected time steps, 2 mL aliquots of the acidic leachates were extracted. Therefore, 10% of the acid leachate volume was removed during each sampling step. Each 2 mL aliquot was centrifuged at 4500 rpm for 15 min, filtered (0.45 μm), evaporated at 90 °C, and re-dissolved in 3% HNO_3 + 0.01 M HF before bulk elemental and isotopic analyses.

3.3. Elemental analyses of the leachates

The Sb concentrations in the leachates were analyzed with inductively-coupled plasma mass spectrometer (ICP-MS; Element-XR, Thermo Scientific) at the Institute of Earth System Sciences, Leibniz University Hannover (Germany). The ICP-MS was equipped with a double-pass quartz glass spray chamber (Scott design, Thermo-Scientific), Ni H-type sample, and skimmer cone. The oxidation rate (U/UO ratio) and the performance of the Element XR were optimized by using a 1 ng/g tune solution to yield a sensitivity of at least 10^5, 10^6, and 1.6×10^6 counts per second (cps) on ^{7}Li, ^{115}In, and ^{238}U in low resolution (LR) mode with oxide (UO) rate lower than 4.5%.

Typically, sample solutions in 3% HNO_3 + traces of HF were doped with ~5 ng/g In as an internal standard. An equal amount of the internal standard with ~5 ng/g In was added to the calibration and background solutions. Raw data were converted to elemental concentrations by a gravimetric five-point calibration. The concentration range covered by the calibration was 0.5 to 90 ng/mL.

Before each analysis, the sample introduction system was rinsed for at least two minutes with 5% HNO_3. The background solution that was doped with the internal standard was measured prior the calibration and sample solutions, to subtract the instrumental background from the measurement signal, although the contribution of the background on Sb and In was generally negligible. The reproducibility was better than 5% (2SD).

3.4. Bulk Sb isotope analyses with solution nebulization MC-ICP-MS

Bulk Sb isotope solution analyses were conducted at the Leibniz Universität Hannover with a Thermo-Scientific Neptune Plus multi-collector ICP-MS (MC-ICP-MS). The sample introduction system included a desolvation unit of a Cetac Aridus-II in combination with a PFA nebulizer with a sampling rate of 100 μL/min. In addition, an Al sampler and skimmer H-cones were used, leading to a ~ 13 V signal on ^{121}Sb in low-mass resolution with a 70 ng/mL Sb solution.

To correct for the instrumental mass bias, all samples and standards were doped with a NIST SRM 3161a Sn standard solution with an assumed ^{119}Sn/^{117}Sn ratio of 1.118421. This ratio was then used to calculate the mass fractionation correction factor β using the exponential law (see Kaufmann et al., 2021).

Analyses were performed sequentially, by using a sample-standard bracketing protocol, relative to NIST SRM 3102a as the Sb standard, according to.

$$\delta^{123}Sb = \left[\left(\left(^{123}Sb/^{121}Sb\right)_{sample} \Big/ \left(^{123}Sb/^{121}Sb\right)_{standard}\right) - 1\right] * 1000 \quad (1)$$

The reproducibility and accuracy were determined by replicate analyses of the in-house Sb standards MAC (0.590 ± 0.023‰), VWR (0.093 ± 0.036‰), MET (0.165 ± 0.041‰), and SC (−0.210 ± 0.044‰) relative to NIST SRM 3102a during each analysis session, which agreed with previously reported literature values (Kaufmann et al., 2021), within uncertainties.

3.5. In-situ Sb isotope analyses with fs-LA-MC-ICP-MS

In-situ Sb isotope analyses were carried out on polished sections with a variety of primary (i.e., stibnite) and secondary minerals, following the protocol described in detail by Kaufmann et al. (2021). In brief, in-situ isotope measurements were performed using an inhouse build-femtosecond laser ablation system (based on a Spectra-Physics Solstice, USA) coupled to MC-ICP-MS (Thermo-Scientific Neptune Plus) at the Leibniz University Hannover (Germany) described in detail by Horn and von Blanckenburg (2007) and Lazarov and Horn (2015). The instrumental mass bias for Sb analyses was monitored using sample-standard bracketing and the analyzed Sn isotope ratios of a simultaneously aspirated Sn standard solution (NIST SRM 3161a, 1 ppm), respectively (Tanimizu et al., 2011). The Sn standard solution was aspirated at a rate of ~100 μL/min through an ESI PFA-ST nebulizer into a quartz spray chamber. Depending on the mineral grain size and Sb content, spot diameter and repetition rate were chosen between 30 and 60 μm and 4 to 25 Hz, respectively, to provide signal intensities comparable to those of the in-house standard SC. Our previous study (Kaufmann et al., 2021, 2023) showed that Sb isotope ratios can be determined on sulfides, oxides, and elemental antimony and can be analyzed with femtosecond LA-MC-ICP-MS largely without significant matrix effects relative to our synthetic stibnite standard (labeled SC). Therefore, the SC standard was generally used as bracketing standard for the determination of all in-situ Sb isotope compositions according to Eq. (1). Finally, the delta values were converted relative to the commonly used Sb isotope standard NIST SRM 3102a (applying $\delta^{123}Sb_{NIST\ SRM\ 3102a} = \delta^{123}Sb_{SC} - 0.189$; Kaufmann et al., 2021). Hereafter, we will report only the $\delta^{123}Sb_{NIST\ SRM\ 3102a}$ values and refer to them as $\delta^{123}Sb$.

Uncertainties for $\delta^{123}Sb$ values are propagated 2SD including measurement uncertainties of sample and bracketing standard analyses. As an internal control to determine the accuracy and precision of the in-situ acquired Sb isotope data, the in-house standards MAC (Micro-Analysis Consultants Ltd. -Stock No: 45464, lot number: L10S026) and MET (metal, Alfa Aesar, lot number: X0034087–1) Sb standards were monitored. The mean $\delta^{123}Sb$ values of 0.640 ± 0.065 ‰ (2SD) and 0.214 ± 0.011 ‰ (2SD) relative to NIST SRM 3102a for MAC and MET, respectively, obtained over a period of all in situ isotope measurement session, agreed with the $\delta^{123}Sb$ (0.645 ‰ (MAC) and 0.192 ‰ (MET)) values reported in Kaufmann et al. (2021).

4. Results

4.1. Natural samples - petrography and chemical composition

Current weathering inside the mines in Pezinok produces masses and stalactites of iron oxides, ubiquitous gypsum crystals, and brandholzite $[Mg(H_2O)_6[Sb(OH)_6]_2]$ crystals. In the flotation tailings deposited outside of the mines, tripuhyite, Sb oxides, and Fe oxides are present. Brandholzite crystals appear rapidly on walls, stopes, or fragments of the ores inside the mine that expose stibnite mineralization with ferroan dolomite without pyrite but are restricted to parts of the walls that are not in contact with flowing or creeping water. They were found to grow to a full size of up to 1 cm within a few months as euhedral, translucent to transparent, colorless to white, pseudohexagonal and tabular crystals with characteristic striations. Some of the brandholzite crystals are skeletal. They may contain inclusions of Sb oxides and stibnite relics. In this work, brandholzite was identified by its morphology and powder XRD measurements. Electron-microprobe analyses were previously carried out on the same material (Majzlan et al., 2016) but were not

attempted here because earlier studies (Friedrich et al., 2000; Sejkora et al., 2010; Majzlan et al., 2016) have shown that brandholzite is unstable under the electron beam, leading to systematic errors in elemental contents.

In the uppermost layers of the flotation tailings in Pezinok, primary minerals were subjected to weathering over the last 40 years. The finely ground primary minerals were converted to secondary minerals in the form of pseudomorphs or authigenic Fe-As-Sb phases (Figs. 1, 2). The secondary minerals occur either as oxidation rims around the primary sulfides (Fig. 1) or as compact (Fig. 2a) or porous (Figs. 2b,d) individual grains without relics of the precursor minerals. In the tailings, Sb enriched rims developed mainly around pyrite and arsenopyrite (Fig. 1). Relics of the primary Sb sulfides, armored by their weathering products, were found only rarely. Secondary minerals may coat other secondary minerals (Fig. 2b) or gangue minerals (Fig. 2c). In some of the grains, substantial porosity witnesses loss of material during weathering (Fig. 2d). The identification of the secondary minerals in the tailings in Pezinok relies on their EMP analyses (this work) and previous extensive work by Lalinská-Voleková et al. (2012). In Fig. 3, all chemical analyses (about 1600 EMP analyses from Lalinská-Voleková et al., 2012) are depicted by the gray field. The micro-X-ray diffraction (μ-XRD) experiments performed in that work delineated fields of several minerals, color-coded in Fig. 3. EMP analyses showed large chemical variations in the Fe, Sb, and As. The Fe_2O_3, Sb_2O_5, and As_2O_5 content varied between 0.65 and 70.34 wt%, 3.34–62.10 wt%, and < 0.1–6.96 wt%, respectively (Table S1). The Fe/(Fe + Sb) ratio of the analyzed minerals ranges between 0.04 and 0.98 with a median of 0.55. It can be seen that the phases with high Fe/(Fe + Sb) ratios, analyzed in this work, fall in the field of Fe oxides (ferrihydrite or goethite). The phases with intermediate Fe/(Fe + Sb) ratios fall in the field of tripuhyite. We note that some of the minerals with similar Fe/(Fe + Sb) ratios analyzed by Lalinská-Voleková et al. (2012) were identified as roméite. In our samples, however, the Ca concentration in each analyzed grain is much too low for romeite (Table S1). Two grains with the lowest Fe/(Fe + Sb) ratios fall in the small field of Sb oxides (cervantite or senarmonite). In the following discussion, we use the mineralogical observations from Lalinská-Voleková et al. (2012), done on the same samples as those used in this work, apply also to the grains analyzed in this work. A more detailed description of the secondary Sb minerals is presented in the works of Lalinská-Voleková et al. (2012), Majzlan et al. (2011) and Majzlan et al. (2016).

At the dumps in Dobšiná, hand specimens of stibnite weather to yellowish masses of secondary minerals. EMP analyses showed that the secondary minerals consist mostly of Sb oxides, with little to negligible content of other elements (Table S1). The low totals in some of the analyses suggest that the material is fine-grained and porous, possibly also hydrated. Powder X-ray diffraction identified valentinite [Sb_2O_3], senarmontite [Sb_2O_3], and cervantite [Sb_2O_4] in approximately equal proportions. A mineral of the roméite group, likely stibiconite [Sb_3O_6OH], is also present, but in amount of <5%. Spatial differentiation of the Sb oxides directly in the polished section used for the isotopic measurements turned out to be not feasible. The reason is strong fluorescence signal in the Raman spectra, coming from the epoxy in the pores of the fine-grained weathering material.

In the Allchar deposit, the soils and dumps are composed mainly of dolomite, quartz, gypsum, pyrite, marcasite, and stibnite. In the dumps, the relics of stibnite are coated by a secondary Fe—Sb product (Fig. 2e). EMP analyses showed that the secondary mineral contains predominantly Fe, Sb, As, with little S. The Fe_2O_3, Sb_2O_5, and As_2O_5 content varied between 25.96 and 40.80 wt%, 44.24–61.86 wt%, and 5.19–8.54 wt%, respectively (Table S1). The Fe/(Fe + Sb) ratio of the analyzed minerals ranges between 0.46 and 0.65, indicating along with Raman shifts (Supplement 3) that the rims around stibnite consist of hydroxyferroroméite (Fig. 2e).

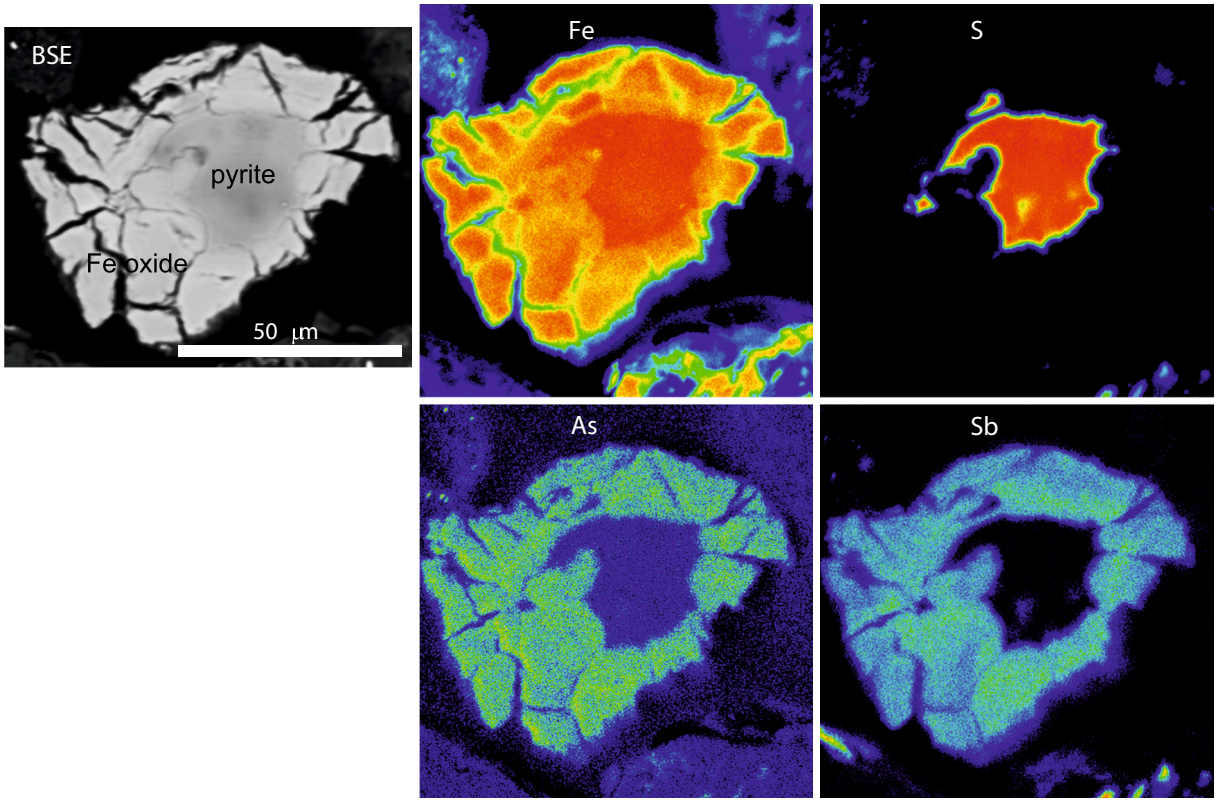

Fig. 1. A weathering grain of pyrite with a thick rim of Fe oxides. Note the absence of As and Sb in pyrite but their abundance in the Fe oxides. Both elements, As and Sb, were enriched in the secondary Fe oxides by adsorption from the pore fluids in the tailing pond. Shown here is the back-scattered electron image of the measured grain and false-color maps of the concentrations of Fe, S, As, and Sb in this grain. The image and data from electron-microprobe measurements.

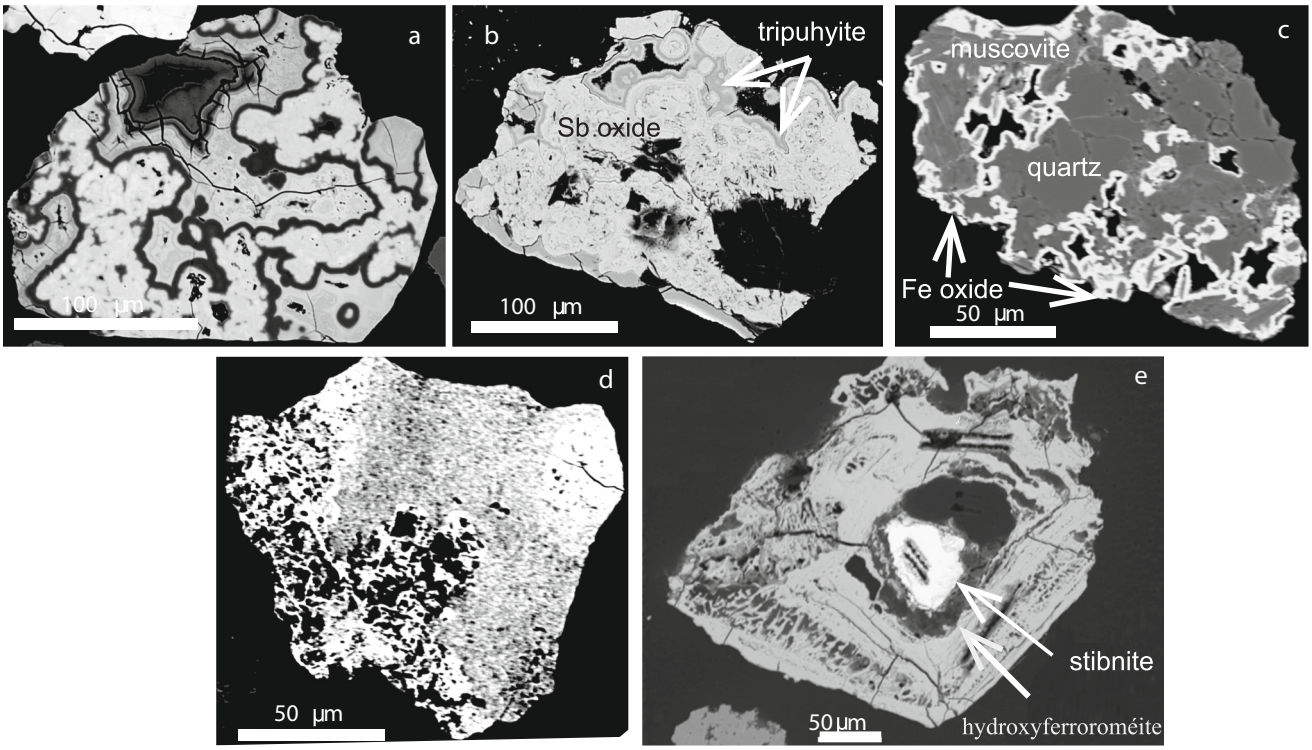

Fig. 2. Back-scattered electron (BSE) images of weathering products from the tailings in Pezinok (a-d): a) Complex zoned overgrowths of poorly crystalline tripuhyite (lighter shades of gray) and Fe oxides (darker), b) Porous Sb oxides overgrown by compact and acicular tripuhyite, c) A grain of quartz and muscovite coated by Fe oxides, d) Porous Sb oxides with visible loss of material, probably a pseudomorph after stibnite; and in Allchar: e) Stibnite rimmed by tripuhyite.

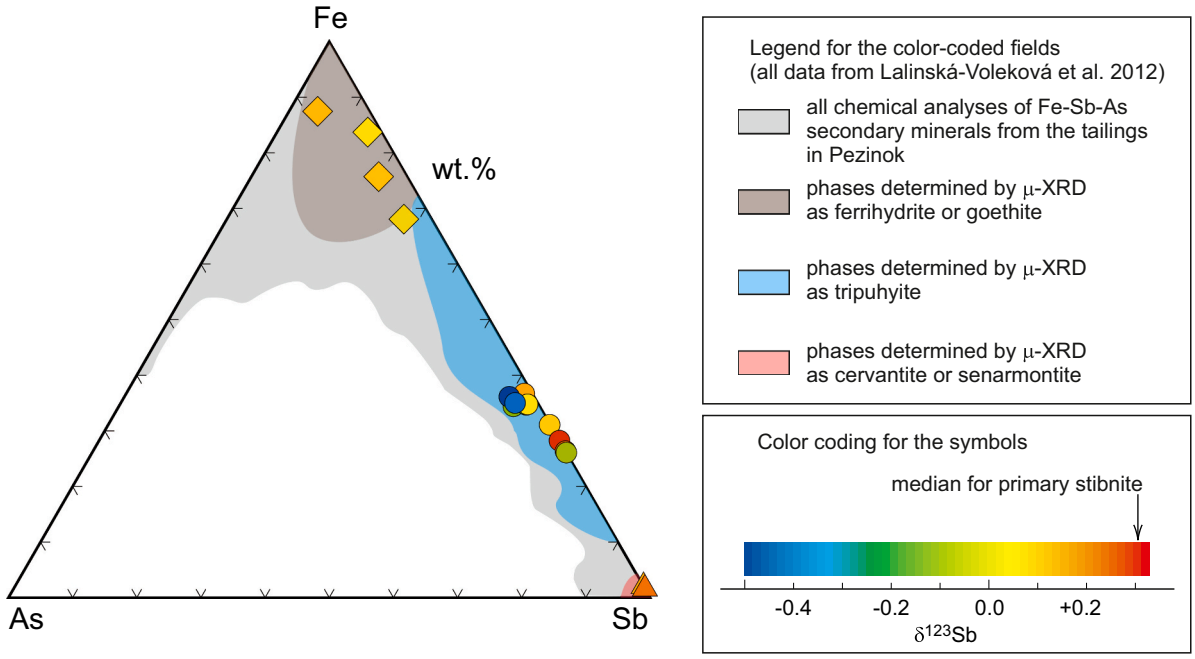

Fig. 3. Triangular Fe-As-Sb diagram with the composition of secondary Fe-Sb-As phases from the tailings in Pezinok. The symbols correspond to the grains analyzed in this work by EMP for their chemical composition and LA-ICP-MS for their Sb isotopic composition. The shape of these symbols relates to Fe oxides (ferrihydrite or goethite; diamonds), tripuhyite (circles), or Sb oxides (cervantite or senarmontite; triangles). The isotopic composition (as δ^{123}Sb) in each measured point is expressed by a color of each symbol and shown by the color scale in the lower right corner. The meaning of the color-coded fields is explained in the legend and in the text.

4.2. Antimony isotopes ($\delta^{123}Sb$) of the secondary Sb minerals

The $\delta^{123}Sb$ values for the investigated minerals in Pezinok are given in Tables S1 and illustrated in Fig. 4 along with the data for the primary stibnite (in Fig. 4 abbreviated as sbn). Secondary minerals in the mine and the mine tailings in Pezinok show an isotopic range of almost 1.2 ‰ ranging from −0.50 to 0.69 ‰ (Figs. 4, 5). Chapmanite (cpm) from Pezinok shows a marked difference relative to the primary stibnite, with $\delta^{123}Sb$ values of −0.27 ± 0.02 ‰ (2SD). In contrast, the average isotopic composition of brandholzite (bdh) is indistinguishable from the average isotopic composition of the primary stibnite determined in a previous study (Kaufmann et al., 2023) at the same location. In one sample, $\delta^{123}Sb$ of brandholzite varies between 0.33 and 0.45 ‰ (n = 7) and Sb oxide inclusions in brandholzite are isotopically 0.3 ‰ heavier than the host. In another sample, the $\delta^{123}Sb$ of brandholzite is 0.06 to 0.17 ‰ (n = 7), essentially indistinguishable from the isotopic composition of the stibnite relics (0.13 ± 0.07 ‰ (2σ)) enclosed in the brandholzite crystals.

In Pezinok, two Sb oxide grains (labeled as Sb oxide in Figs. 4, 5) with a low Fe/(Fe + Sb) ratio of 0.05 had isotope values close to 0.20 ‰, with elevated Al_2O_3 (14.0–16.8 wt%) and low As_2O_5 (<0.25 wt%). The majority of oxide grains with Fe/(Fe + Sb) ratios between 0.42 and 0.67 belong to tripuhyite (tpy). They are characterized by large isotopic variations (−0.50 to 0.29 ‰, median = −0.01 ‰) with a shift towards lower $\delta^{123}Sb$ compared to the primary stibnite (median = 0.31 ‰, Kaufmann et al., 2023). Phases with Fe/(Fe + Sb) > 0.84 and lower Sb content (2–16 wt%) belong to Fe oxides (in Figs. 4, 5 labeled as Fe oxide) and have isotopic values between −0.01 and 0.13 ‰.

The Sb oxide crust on stibnite from the Dobšiná deposit is marked by an isotopic range between −0.12 to −0.05 ‰ (Table S1, Fig. 4). Stibnite in the same section as the Sb oxides showed $\delta^{123}Sb$ values between 0.00 ‰ at the rim (sbn rim) to 0.09 ‰ in the center (in Fig. 4 abbreviated as sbn core; Fig. 6). Small stibnite grains (<100 μm; in Fig. 5 described as sbn s) in the Sb oxides show indistinguishable isotope values (−0.1 to −0.05 ‰) relative to those of the surrounding Sb oxides. The available data indicate that the isotopic composition changes progressively from the center to the rim within stibnite grains (Fig. 4).

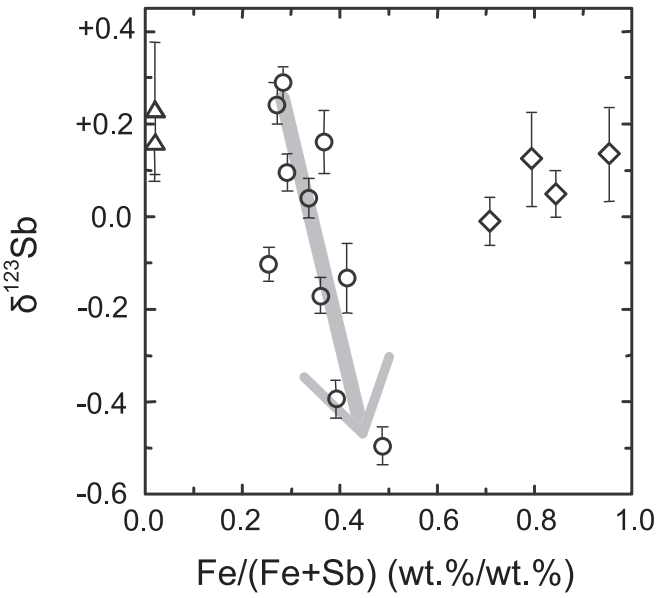

Fig. 5. Fe/(Fe + Sb) ratio of the secondary Fe-Sb-As phases in the tailings in Pezinok versus their $\delta^{123}Sb$ values. Circles = tripuhyite; triangles = Sb oxides; diamonds = Fe oxides. All data in Table S1.

The analyzed stibnite relics (in Fig. 4 = sbn) from the Allchar deposit show a large isotopic variation ranging from 0.15 to 0.88 ‰, while Fe—Sb oxides have $\delta^{123}Sb$ values between −0.05 and 0.58 ‰ (Table S1). Spatially associated stibnite and Fe—Sb oxides, on the scale of hundreds of micrometers, display an almost constant isotopic offset with secondary products being consistently isotopically lighter than the stibnite by 0.2 to 0.3 ‰. (Fig. 4).

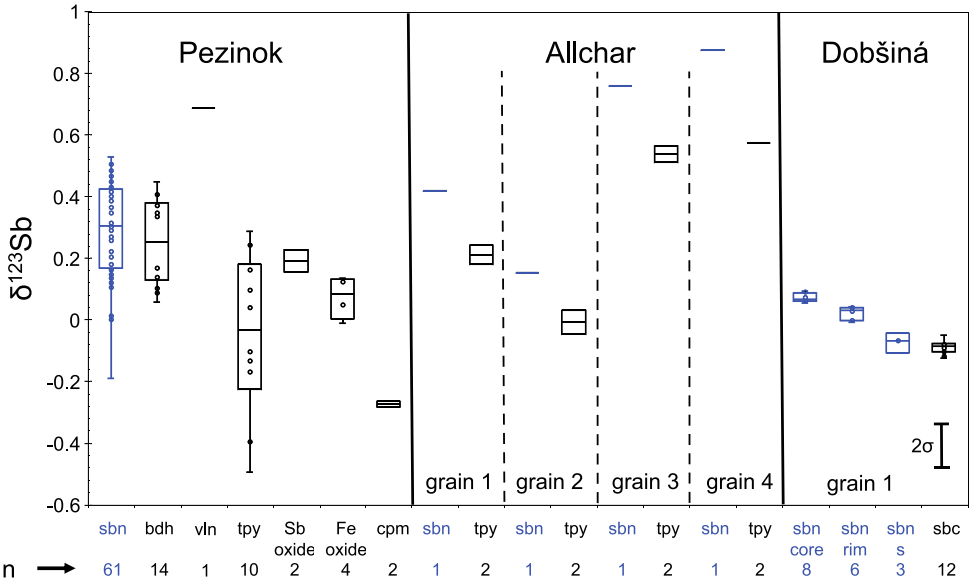

Fig. 4. A box plot showing $\delta^{123}Sb$ values of the primary stibnite (data from Pezinok taken from Kaufmann et al., 2023) and secondary Sb minerals measured in this work. All measurement results are expressed relative to NIST SRM 3102a (Kaufmann et al., 2021) Sb standard. The box and whiskers show the 5th, 25th, 75th, and 95th percentiles. Within the box, the horizontal line represents the mean. Abbreviations: sbn = stibnite; bdh = brandholzite; vln = valentinite; tpy = tripuyhite; cpm = chapmanite. Primary minerals are marked by blue color. Secondary Sb minerals (bdh, vln, tpy, Sb oxide, Fe oxide, and cpm) from Pezinok are related to the average Sb isotopic composition of stibnite, while the secondary minerals from Dobšiná and Allchar are related to specific stibnite grain in the same hand specimen. Representative 2σ error bars are given in the.
lower right corner, corresponding to the average error-propagated internal uncertainties (2 SE) of the sample and standard measurements (calculated as described by Horn et al. (2006)). (For interpretation of the references to color in this figure legend, the reader is referred to the web version of this article.)

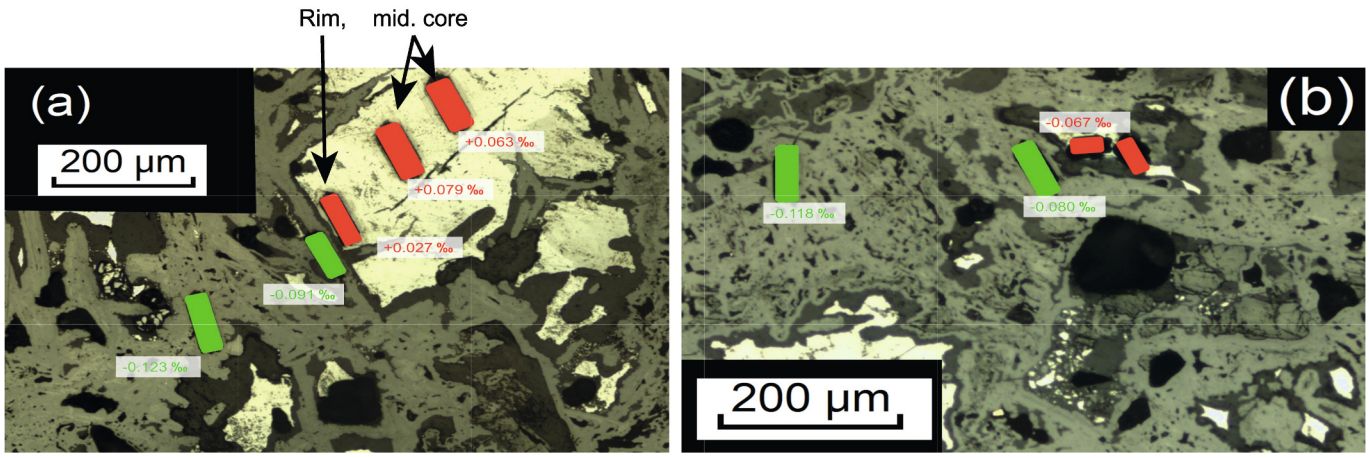

Fig. 6. Microscopic images of laser line analyses of stibnite (red lines) that is surrounded by Sb oxides (green lines). Sample from Dobšiná. (a) Isotopic analyses at different distances between Sb oxides and stibnite interface. (b) Small stibnite relics (abbreviated as "sbn s" in Fig. 4) are surrounded by secondary Sb oxides. (For interpretation of the references to color in this figure legend, the reader is referred to the web version of this article.)

4.3. Leaching experiment

The aqueous Sb concentration increased progressively during the batch leaching experiments and reached up to 1% of the total Sb content of the stibnite sample (Fig. 7a). The absolute amount of Sb released into the leachate from stibnite, for the three different acids was small, 0.52 mg (oxalic acid), 1.01 mg (0.05 M HCl) to 1.68 mg (0.5 M HNO_3) compared to 72 mg of Sb in stibnite (Table S2). Therefore, the isotopic composition of the leached stibnite residue was not analyzed as we assumed that the bulk isotope composition of the stibnite remained essentially unaffected. In the leaching experiment, the Sb leached into the first extracted aliquot was generally isotopically heavier than the Sb in the stibnite. During progressive leaching with HCl and oxalic acid, the leachate became isotopically heavier with a maximum at around 90 h (oxalic acid and HCl) and then scattered and became lighter until the end of the experiment. The leachate with HNO_3 remained essentially isotopically constant (Table S2). The aliquots with <50 µg Sb mL^{-1} (i.e. with mobilization of <0.05% of the initial Sb in stibnite) were usually isotopically heavier than the stibnite, whereas those with higher Sb concentrations are isotopically comparable to the starting stibnite solid (green bar in Fig. 7b). At the start and end of the leaching experiment, the oxidation-reduction potential (ORP) and pH values were measured. The ORP and pH values ranged from 563 to 677 mV, and 1.4 to 1.8, respectively, for leaching with 0.05 M HCl. A higher ORP (634–733 mV) and lower pH (0.7–1.2) was measured during the batch leaching experiment with 0.5 M HNO_3. More variation in ORP (585–863 mV) at almost constant pH (1.4–1.6) was measured during leaching with 0.1 M oxalic acid.

5. Discussion

5.1. Stibnite dissolution - leaching experiment

Our leaching experiment demonstrated a δ^{123}Sb difference of up to +0.5 ‰ (Fig. 7b) for Sb in the aqueous phase relative to that of the dissolving solid, i.e., the stibnite sample. The most important result of this experiment is that progressive leaching with HCl, HNO_3, and oxalic acid results in a preferential enrichment of the heavy Sb isotopes in the leachate. Variations caused by isotopic heterogeneity of the starting material can be excluded because the stibnite sample used was shown to be chemically and isotopically homogeneous (Kaufmann et al., 2021). Although we cannot exclude that an oxidation film was formed over time on the stibnite powder used in this experiment, it appears unlikely due to the cautious storage in a container with limited oxygen entry.

During the first ~51.5 h of the experiment (collection of the first 6 samples), only limited Sb isotope fractionation was observed (Fig. 7b). These results suggest that the strong acids quantitatively removed successive surface layers from stibnite without isotope fractionation. By then, repeated sample collecting resulted in a decrease of the initial acid volume by ~50%. Subsequently, we observed stronger isotopic fractionation and stronger variation in Sb concentrations.

As a redox-sensitive element, Sb attains usually the oxidation states of Sb^{3+} and Sb^{5+}. During the oxidative dissolution of stibnite, sulfur is oxidized to sulfate and Sb is mobilized as $Sb^{3+}(OH)_3$ (Biver and Shotyk, 2012):

$$Sb_2S_3(s) + 6O_2\ (aq) + 6H_2O\ (l) \rightarrow 2Sb(OH)_3(aq) + 3H_2SO_4(aq) \quad (2)$$

In this reaction, the oxidation of sulfur precedes that of Sb. The dissolved Sb^{3+} can be further oxidized as (Hu et al., 2015).

$$2Sb(OH)_3\ (aq) + O_2\ (aq) + 4H_2O\ (l) \rightarrow 2Sb(OH)_6^-\ (aq) + 2H^+\ (aq) \quad (3)$$

The oxidation rates in strongly acidic media, such as those used in this work, are not known. It is known, though, that abiotic Sb oxidation is kinetically limited in natural waters with typical H_2O_2 concentrations (10^{-6} M to 10^{-8} M) neutral (pH ~7), and alkaline (pH ~9) with a half-life between 11 days to 324 years (Leuz and Johnson, 2005; Asta et al., 2012; Biver and Shotyk, 2012; Loni et al., 2020). In the upper 100 m of the Black Sea, Cutter (1992) reported residence times for Sb^{3+}, before it is oxidized to Sb^{5+}, of about 125 days (transformation rate: 0.008 day^{-1}). The oxidation rate for the Black Sea, in comparison to experimental data of Leuz and Johnson (2005), is accelerated by adsorption and biotic uptake processes (Cutter, 1992). The duration of our leaching experiment (168 h = 7 days) is on the lower end of the half-life ranges for Sb oxidation reported in the literature. It is unclear if Sb oxidation occurred in our experiment or not.

In the abiotic experiments in HCl, Ferrari et al. (2023) showed that during Sb oxidation, small Sb isotope fractionation of 0.3‰ occurs, resulting in Sb^{5+} species being enriched in the heavier ^{123}Sb isotope. The experiments of Ferrari et al. (2023) were, however, conducted in the presence of H_2O_2 that enormously increased the oxidation rate of Sb. This was not the case for our experimental approach, and we thus assume that an effect other than Sb oxidation caused the isotope fractionation. The experiments by Ferrari et al. (2024) showed an enrichment of the light Sb isotope during adsorption on schwertmannite and ferrihydrite with no dependence of the pH, Fe—Sb ratio or Sb oxidation state (3+ versus 5+). It is not clear, however, if the principal process in these experiments was adsorption (e.g., adsorption of a monolayer) or surface precipitation. The isotopic fractionation during adsorption processes was found to be similar for Sb^{3+} and Sb^{5+} (Ferrari et al., 2024). These authors investigated adsorption of the species with

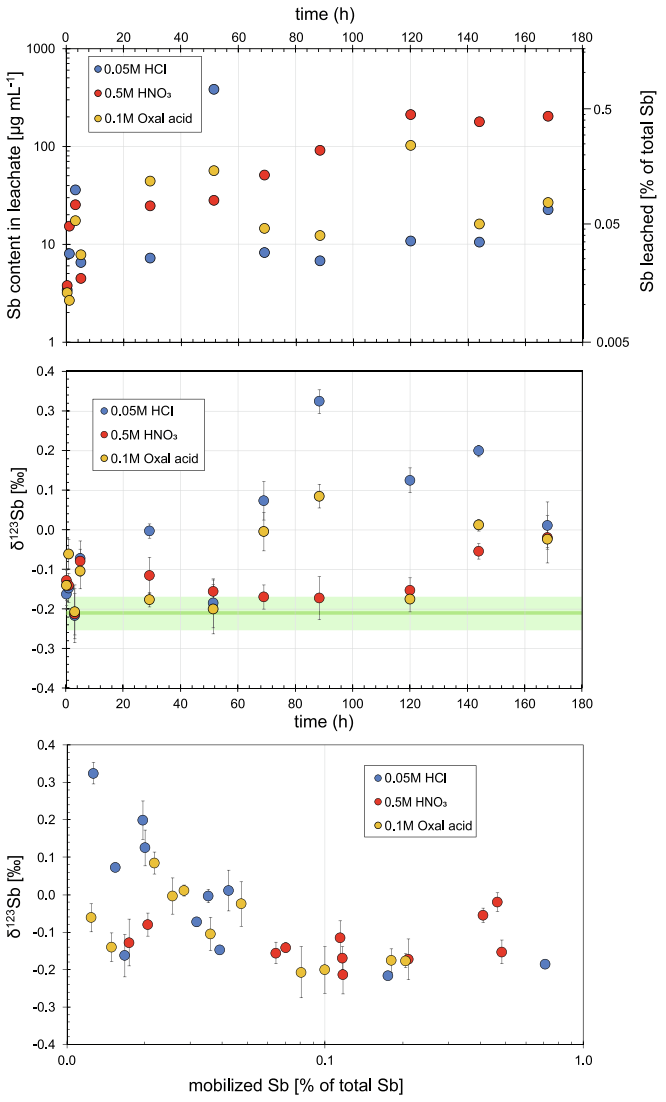

Fig. 7. Stibnite batch leaching experiment with 0.05 M HCl, 0.5 M HNO_3, and 0.1 M oxalic acid. Time resolved antimony concentrations (a) and isotope composition (b) and concentration vs. isotope composition (c). The green bar represents the average isotopic composition with the analytical uncertainties of the leached stibnite measured throughout this study. All δ^{123}Sb measurements are expressed relative to NIST SRM 3102a and the error bars correspond to the 2SD of replicate analyses of the same solutions. (For interpretation of the references to color in this figure legend, the reader is referred to the web version of this article.)

both oxidation states on ferrihydrite and schwertmannite. Our leaching experiment included only pure stibnite and no other solid phases such as clays, Fe, or Mn oxides, that are well known as substrates for Sb adsorption (Luo et al., 2023; Zhou et al., 2023; Ferrari et al., 2024; Wu et al., 2024). Therefore, in our experiment, surface precipitation controlled the transfer of Sb from the solution to the solid, and adsorption did not play a decisive role.

The scattered decline of dissolved Sb at the end of the experiments (for HCl and oxalic acid leaching) and the negative correlation of the dissolved Sb concentrations and its isotope composition can be interpreted as a result of precipitation of secondary Sb minerals. Likely, such a process would be kinetically driven, resulting in kinetic isotope fractionation and thus, leading to the preferential removal of light Sb isotopes from the solution. Such a scenario may explain well the observation of high δ^{123}Sb combined with a decrease of the Sb concentration at the end of the HCl and oxalic acid leaching experiments.

The feasibility of precipitation from leachate can be best described by the saturation indices (SI) that depend on the ORP, pH values, and Sb molality, related to the reaction $2Sb(OH)_3^0 \rightarrow Sb_2O_3 + 3H_2O$. Simulations with the PHREEQC software (Parkhurst and Appelo, 1999) showed that the solutions are undersatured with respect to Sb_2O_3 in the initial stages of the experiment. As the experiment progresses, the Sb molality is increasing (Fig. 7a) and the ORP is decreasing, likely as a response of the oxidation of sulfide to sulfate. Both of these changes modify the saturation indices with respect to Sb_2O_3. Eventually, all acidic leachates were supersaturated with respect to senarmontite (cubic Sb_2O_3). Hence, the calculated saturation indices confirm that senarmontite could precipitate during the leaching experiment and draw Sb out of the solution.

The most plausible explanation of our experimental results, both chemical (Fig. 7a) and isotopic (Fig. 7b), is the combination of oxidative dissolution and precipitation of Sb^{3+} oxides. The enrichment of the heavy Sb isotopes in the leachate is assigned to both processes. The first, insignificant effect of oxidation of Sb^{3+} to Sb^{5+} (reaction 2), induces only minor isotopic fractionation (as also observed by Ferrari et al., 2023), during which the more soluble Sb^{5+} pool harvests the heavier isotopes. The second one is of much greater magnitude, and it is the precipitation of Sb^{3+} oxides (e.g., senarmontite). Such rapid precipitation can, for kinetic reasons, draw lighter Sb isotopes from the solution into the precipitating solid.

5.2. Comparison to isotopic changes during leaching of stibnite and other minerals

Isotopic trends during similar leaching experiments (with pH values ranging between 2 and 5.2) were observed in the case of Cu (in chalcopyrite), Fe (in pyrite and goethite), and Zn (in sphalerite) by Fernandez and Borrok (2009), Mathur et al. (2005), Wiederhold et al. (2006), Kiczka et al. (2010) or Kimball et al. (2009). In the absence of microorganisms, Fernandez and Borrok (2009), Mathur et al. (2005), and Kimball et al. (2009), observed that the initial isotopic composition (expressed as δ values) of the leachate was higher (i.e., isotopically heavier) than in the starting material. With time, however, the δ values decreased as the leaching progressed and dropped back to δ values comparable to those in the leached solids. This isotopic trend was explained by the leaching of a pre-existing oxidized layer on the surface, causing the preferential transfer of the heavy isotopes from the surface layer into the aqueous medium. As leaching and decomposition proceeded, the leachate returned isotopically to the composition of the source mineral (Kimball et al., 2009; Fernandez and Borrok, 2009). This observation suggests that for the pristine primary mineral, the dissolution itself proceeds as a moving reaction front and is limited to a reactive surface layer. Therefore, dissolution itself can be described as a bulk process, without significant isotopic fractionation.

For stibnite, the interplay of dissolution, redox changes in the aqueous medium, and precipitation of secondary phases causes the enrichment of the leachate in the heavy Sb isotopes. This finding is important inasmuch that many of the observations on the natural samples can be rationalized by such a trend. We do note, however, that the acids and their molarities used in this study do not correspond to those encountered in field settings. The choice of the acids and their molarity was dictated by the need to complete the experiments within a reasonable time rather than mimic the natural conditions accurately.

5.3. In situ weathering and replacement of stibnite

The primary minerals in Pezinok are marked by a large isotopic range between −0.4 to 0.8 ‰, with lower δ^{123}Sb values in the paragenetically early sulfides and higher δ^{123}Sb in the later sulfides and oxides (Kaufmann et al., 2023). For this work, however, not all primary minerals are of interest, simply because most of them are not abundant. Stibnite dominates the ores and has a δ^{123}Sb median of 0.31 ‰, with a range of −0.19 to 0.53 ‰. The other primary minerals are of too little

abundance to contribute much to the Sb isotopic budget in the weathering products. Therefore, in the absence of a direct relationship between primary to secondary minerals, we will compare the median isotope composition 0.31 ‰ of the stibnite as the initial isotope composition to all secondary minerals.

5.3.1. Isotopic fractionation in the pseudomorphs of Sb oxides after stibnite in tailings

Based on textural evidence, some of the grains in the tailings in Pezinok were interpreted as pseudomorphs after stibnite by Majzlan et al. (2011) and also in this work (Figs. 2b,d). In terms of their mineralogy, they belong to Sb oxides, either cervantite or senarmontite (Fig. 3, Lalinská-Voleková et al., 2012). The δ^{123}Sb values of these Sb oxides range between 0.16 ‰ and 0.23 ‰ and show no substantial isotopic differences to stibnite. Hence, in this case, stibnite is transformed completely into secondary products, but Sb is either not oxidized at all (in senarmontite, Sb_2O_3) or only partially oxidized (in cervantite, Sb_2O_4). The porosity of the Sb oxides (Fig. 2d) does not necessarily result from the loss of Sb. When considering their molar volumes, the conversion of stibnite to senarmontite with complete retention of Sb would mean a volume loss of almost 50%. Therefore, we assume that the Sb oxides formed by a rapid solid-state transformation (S—O exchange) of stibnite with or without partial Sb oxidation, possibly accompanied by a small loss of Sb. The weathering in the tailings is fast because the grains are small (ground in the technological process to 40–90 μm; Grexová, 1991) and exposed to the oxidizing environment in the uppermost tailings layer (Maruška et al., 2000). In such a scenario, the Sb oxides retain essentially the isotopic signature of the parent stibnite. A small shift to lower δ^{123}Sb values could have occurred during the process of partial dissolution of stibnite and subsequent reprecipitation of Sb oxides. Such a shift is in agreement with the results of our leaching experiment. It shows that the stibnite dissolution leads to supersaturation of the solution with respect to Sb secondary phases, resulting in their precipitations, likely associated with kinetically-driven isotope fractionation, with preferential precipitation of light isotopes.

5.3.2. Isotopic fractionation in the crusts of Sb oxides on stibnite in dumps

A different pattern of Sb isotopic composition is observed on large stibnite pieces (centimeter to decimeter size) found on dumps, such as the dump in Dobšiná and Allchar investigated in this work. Such pieces are exposed to precipitation and flushing with water (e.g., during snow melting) over long time, sometimes over decades or centuries. The Sb oxides armor the primary stibnite, form crusts of millimeter to centimeter thickness, and decelerate weathering of stibnite.

In this case, the isotopic composition of both primary stibnite and its secondary weathering products can be measured (Figs. 4, 6). In the Dobšiná samples, there is a clear spatial trend of decreasing δ^{123}Sb values away from the stibnite relics. The δ^{123}Sb values in the central parts of the stibnite relics (0.06 ‰ to 0.09 ‰) are slightly higher than the outer rims of stibnite (−0.01 ‰ to 0.04 ‰). Those are, in turn, higher than the values measured in the secondary Sb oxides (−0.05 ‰ to −0.12 ‰) (Fig. 4).

In the Allchar samples, similar isotopic differences as in the Dobšiná samples were observed. Despite the pronounced variations of the δ^{123}Sb in the primary stibnite, the secondary products on each particular stibnite grain are consistently isotopically lighter. Independently of the thickness of the secondary rim, a constant $\Delta^{123}Sb_{\text{stibnite-secondary product}}$ of ~0.2 ‰ (Fig. 6) was determined.

The leaching experiment discussed in the previous section also showed a preferential enrichment of the heavy isotope in the leachate. We assigned the observed isotopic fractionation predominantly to the precipitation of the secondary products from the supersaturated aqueous solution (SI with respect to senarmontite from the first to last leachate: −1.36 to 1.87 (0.05 M HCl); −3.36 to −1.40 (0.5 M HNO_3); −16.08 to 0.15 (0.1 M oxalic acid). Such a process likely also operates in nature; the secondary Sb minerals at the studied and many other localities testify that the percolating solutions had to be supersaturated with respect to Sb oxides or Fe-Sb-Ca phases. Hence, we propose that a similar process leads to the observed isotopic variations, namely oxidative dissolution of stibnite without significant isotopic fractionation, followed by precipitation of secondary minerals. The latter is likely a kinetically driven process, resulting in isotopically light solids and removal of isotopically heavy solution.

5.3.3. Isotopic fractionation during natural leaching of stibnite and conversion to secondary Sb minerals

Unlike in the two previous cases, stibnite can be leached and converted to secondary minerals also by purely natural processes, without previous excavation of ores and deposition of mining waste. An example thereof is the occurrence of chapmanite in one of the adits in Pezinok. Textural evidence suggests that chapmanite formed together with siderite, pyrite, and cryptocrystalline silica under near-neutral or slightly alkaline conditions from lukewarm fluids (Majzlan et al., 2021). Chapmanite has markedly lighter δ^{123}Sb value of −0.27‰ than the primary stibnite in Pezinok (median δ^{123}Sb = 0.31 ‰).

The large isotopic difference and its direction may be explained by prolonged replacement of stibnite by chapmanite and removal of the heavy isotopes into the circulating fluid, likely, as a result of kinetic isotope fractionation during the formation of the chapmanite (as discussed above). The large isotope effects, observed here, indicate that only a fraction of the dissolved Sb re-precipitated as chapmanite. Chapmanite is therefore the isotopically light leftover of the prolonged natural leaching and transformation of stibnite, essentially an end member of the process captured in the previous case of stibnite weathering to Sb oxides (localities Dobšiná and Allchar).

5.3.4. Isotope fractionation during dissolution, transport, and reprecipitation processes

5.3.4.1. Isotopic fractionation during crystallization of brandholzite. Brandholzite forms by concomitant dissolution of stibnite and ferroan dolomite and crystallization from a thin water film on the walls of the old mines (Majzlan et al., 2016). High aqueous Ca^{2+} and Mg^{2+} concentrations, derived from the dolomite, at near-neutral pH conditions accelerate the dissolution of stibnite (Biver and Shotyk, 2012). Brandholzite does not form if the mineral assemblage that weathering is rich in pyrite (because of the generated acidity) or if the aqueous solutions are voluminous (such as flowing water, because of dilution effects) (Majzlan et al., 2016; Radková et al., 2020). Therefore, the formation of brandholzite is commonly restricted to a thin film of condensed water close to the primary stibnite and dolomite. Brandholzite forms rapidly, within weeks or months, in the open spaces of the old adits.

Brandholzite is isotopically (median + 0.25 ‰) very close to the primary stibnite (median + 0.31 ‰). In contrast to the formation of chapmanite, as discussed above, the very similar isotope composition of the primary and secondary mineral infers that Sb is quantitatively transferred from the reactant (stibnite) into the product (brandholzite). Such a transfer can readily explain the similarity of the δ^{123}Sb isotopic values for the two minerals, regardless of any fractionation that may occur during dissolution of stibnite, redox reaction, or precipitation of brandholzite. The thin water film is fully oxygenated and likely drives the oxidation of Sb^{3+} in stibnite completely to Sb^{5+} in brandholzite. The match of the δ^{123}Sb value is particularly well seen in the samples where brandholzite still encloses stibnite relics. In such a case, brandholzite has identical δ^{123}Sb = 0.12 ± 0.08 (2SD) like the enclosed stibnite δ^{123}Sb = 0.13 ± 0.07 (2σ).

5.3.4.2. Isotopic fractionation during adsorption of Sb. Iron oxides, either ferrihydrite or goethite (Fig. 3) form rims on primary Fe-bearing minerals (mostly pyrite or arsenopyrite, Fig. 1) and on gangue minerals (Fig. 2c), or compact grains without relics of the primary sulfides. Most

of the primary sulfides, such as pyrite or arsenopyrite, are nominally Sb-free but the Fe oxides adsorb copious amounts of the element (Fig. 1, Majzlan et al., 2011). These chemical and textural features are clear evidence of metalloid adsorption onto the Fe oxides. Large Sb isotope fractionation of up to 1.1 ‰ may occur during Sb adsorption on Fe oxides (Zhou et al., 2023; Ferrari et al., 2024), with preferential enrichment of light Sb isotopes in the adsorbate. The magnitude of isotopic fractionation appears also to depend on the chemical composition of the substrate. For example, Zhou et al. (2022) observed no significant isotopic fractionation during Sb adsorption onto Al oxides. The experimental results on adsorption were confirmed in field water system settings at the Xikuangshan mine in China by Wen et al. (2023). They observed an increase of δ^{123}Sb values coupled with a decrease of Sb content in the surface and groundwater samples, interpreted as preferential adsorption of ^{121}Sb onto Fe—Mn oxides. The direction and magnitude of fractionation (Δ^{123}Sb ~ −0.22 ‰) owing to adsorption is consistent with our data, with an average δ^{123}Sb value for the adsorbed Sb on Fe oxides of 0.09 ± 0.14 ‰ (2SD), being lower than the median δ^{123}Sb of stibnite (0.31 ± 0.29 ‰, 2SD). Likely, the dissolved Sb pool in the pore fluid of the tailing pond that was adsorbed to Fe oxides, was already isotopically heavier than the primary δ^{123}Sb of stibnite, because of removal of light Sb isotopes during secondary Sb mineral precipitation. This may explain the relatively small difference between the δ^{123}Sb values of the primary stibnite and that of the Fe oxides with adsorbed Sb, compared to that described in the literature (Zhou et al., 2023; Ferrari et al., 2024).

5.3.4.3. Isotopic fractionation during precipitation of tripuhyite. Tripuhyite from Pezinok displays the most variable δ^{123}Sb of all secondary minerals. The δ^{123}Sb range between values as low as −0.5‰ up to the values similar to those of the primary stibnite, hence, mostly lower than those in the primary stibnite. Tripuhyite forms compact grains, with distinct growth bands (Figs. 2a,b). It was assumed that they precipitate from an aqueous solution that accumulated sufficient Fe^{3+} and Sb^{5+} to be supersaturated with respect to tripuhyite (Majzlan et al., 2011). Yet, more recent calculations of Burton et al. (2020) show that the aqueous molalities of Sb^{5+} would need to be as high as 10^{-3} mol L^{-1} to reach saturation with respect to tripuhyite. Such concentrations cannot be reached in the bulk pore fluid in the tailing pond. This conclusion is supported by the textural observations in the tailings. Tripuhyite was found commonly to form intergrowths with complex banding (Fig. 2a) or overgrowth of secondary Sb oxides (Fig. 2b). It does not, however, coat gangue minerals in the tailings, attesting to the hypothesis that bulk saturation with respect to tripuhyite was not reached. The Fe oxides, on the other hand, commonly coat gangue minerals (Fig. 2c), documenting mobility of Fe in the pore fluid and bulk supersaturation with respect to ferrihydrite or goethite. These observations document that tripuhyite forms at or near dissolving grains of stibnite or secondary Sb oxides, not from the bulk solution, and must inherit its Sb isotopic signature from the dissolving solids, not from the bulk solution in the tailings.

The Sb concentrations necessary to produce tripuhyite could be attained in the vicinity of the dissolving stibnite grains or dissolving secondary Sb oxides. In contrast to the formation of the Sb^{3+} oxides (see above), Sb must be oxidized in this process. Our leaching experiments suggested that the dissolution of stibnite alone results in negligible Sb isotopic fractionation. Instead, supersaturation of the aqueous solution causes precipitation of isotopically light secondary Sb minerals and enrichment of the fluid in the heavy Sb isotope. Oxidation of Sb^{3+} to Sb^{5+} may lead to minor isotope fractionation, confirmed also by density-functional theory calculations and abiotic experiments of Ferrari et al. (2022, 2023). Such oxidation could lead to larger isotopic fractionation in the direction compatible with our observations only if it was kinetically-driven, and for example, carried out by microorganisms (Jia et al., 2024). Another explanation for the low δ^{123}Sb observed for the some tripuhyite grains, coherent with the interpretations provided previously in this work, is kinetic precipitation of Sb phases from the locally supersaturated aqueous solution. Given that the formation of tripuhyite is very slow (years to decades; Majzlan et al., 2016), a viable option is that after stibnite dissolution, isotopically lighter Sb^{3+}-Sb^{5+} oxides (e.g. stibiconite, senarmontite, valentinite) precipitate as intermediate species that are subsequently slowly converted into the less soluble tripuhyite. In either way, the large isotopic range observed for tripuhyite indicates that it likely formed by several simultaneous or subsequent mechanisms, involving multiple steps.

5.4. The tale of light and heavy Sb isotopes

The available data for different natural systems, including hydrothermal ores and mine-affected rivers (Rouxel et al., 2003; Asaoka et al., 2011; Tanimizu et al., 2011; Lobo et al., 2012; Zhai et al., 2021) show a δ^{123}Sb range from −0.4 to 1.8 ‰. The median stibnite δ^{123}Sb are about 0.3 ‰ (Lobo et al., 2012; Zhai et al., 2021), similar to those determined in this work. Based on a single study of Rouxel et al. (2003), seawater appears to be slightly isotopically heavier, with δ^{123}Sb of 0.37 ‰. Markedly heavier values were reported for ground water (0.6%) and some mine drainage waters (up to 0.9 ‰; Tanimizu et al., 2011). From these limited data sets, it appears that surface and ground water are isotopically heavy and that this heavy Sb is transported into the oceans. This scenario is supported by our findings on the behavior of Sb isotopes during stibnite weathering. Weathering of stibnite, by far most common primary Sb mineral, leaves isotopically light Sb secondary minerals at or near the weathering site and an isotopically heavy reservoir that is mobile and transported with the aqueous media. Further research should be focused on these questions: Does the weathering of stibnite (or other Sb sulfides) contribute significantly to the input of Sb in rivers and the oceans or is Sb in rivers dominated by input from weathering of common silicate rocks? These questions relate to some uncertainty in the estimated Sb content in the upper continental crust (Rudnick, 2018). Another question, that needs to be addressed in future studies, is if weathering-related mobilization of Sb changed from pre-industrial to current times and how does it contribute to the concentration and isotopic composition of different surface reservoirs on the Earth.

6. Conclusions

Our study demonstrates that weathering of stibnite can produce isotopic variations of >1 ‰ (from −0.50 to 0.69 ‰) in the secondary Sb minerals. In certain cases, the secondary minerals can be essentially isotopically indistinguishable from the primary minerals. In such cases, they form as pseudomorphs with quantitative transfer of Sb from the source (stibnite) into the secondary Sb product. However, most of the secondary minerals are isotopically lighter compared to the corresponding primary stibnite. Leaching experiments conducted in this study, suggest that the largest isotope effects apparently occur during kinetically-driven precipitation of secondary Sb phases from the dissolving stibnite. This finding explains well the light Sb isotopic range observed for secondary Sb minerals in this study, indicating that the dissolved Sb pool, resulting from weathering of Sb deposits, is likely isotopically heavy.

CRediT authorship contribution statement

Andreas B. Kaufmann: Writing – original draft, Visualization, Validation, Methodology, Investigation, Data curation. **Marina Lazarov:** Writing – original draft, Supervision, Project administration, Investigation, Funding acquisition. **Ingo Horn:** Writing – original draft, Methodology, Investigation. **Martin Števko:** Resources, Investigation. **Tamara Đorđević:** Writing – original draft, Visualization, Resources, Investigation. **Stefan Weyer:** Writing – original draft, Visualization, Validation, Supervision, Project administration, Investigation. **Juraj Majzlan:** Writing – original draft, Visualization, Supervision, Project

administration, Investigation, Funding acquisition, Data curation, Conceptualization.

Declaration of competing interest

The authors declare the following financial interests/personal relationships which may be considered as potential competing interests:

Andreas B. Kaufmann reports financial support was provided by Deutsche Forschungsgemeinschaft LA 3392-3-1 and MA 3927-32-1. Tamara Dordevic reports financial support was provided by Austrian Science Fund P 36828-N. Martin Stevko reports financial support was provided by Slovak Research and Development Agency project No. APVV-22-0041.

Data availability

Data will be made available on request.

Acknowledgements

We thank Oleg Pokrovsky (editor) and five anonymous reviewers for their constructive comments that helped to improve the manuscript. This study was financially supported by the *Deutsche Forschungsgemeinschaft* (grant LA 3392/3-1 and MA 3927/32-1). T. Đorđević gratefully acknowledges the financial support of the Austrian Science Fund (FWF) [P 36828-N]. We express our gratitude to Dr. Wencke Wegner for her valuable assistance during microprobe measurements. M. Števko gratefully acknowledges the financial support of the Slovak Research and Development Agency project No. APVV-22-0041.

Appendix A. Supplementary data

Supplementary data to this article can be found online at https://doi.org/10.1016/j.chemgeo.2024.122253.

References

Akcil, A., Koldas, S., 2006. Acid Mine Drainage (AMD): causes, treatment and case studies. Journal of Cleaner Production 14 (12–13), 1139–1145.

Asaoka, S., Takahashi, Y., Araki, Y., Tanimizu, M., 2011. Preconcentration method of antimony using modified thiol cotton fiber for isotopic analyses of antimony in natural samples. Anal. Sci. Int. J. Jpn. Soc. Anal. Chem. 27 (1), 25–28.

Asta, M.P., Nordstrom, D.K., McCleskey, R.B., 2012. Simultaneous oxidation of arsenic and antimony at low and circumneutral pH, with and without microbial catalysism. Appl. Geochem. 27, 281–291. https://doi.org/10.1016/j.apgeochem.2011.09.002.

Biver, M., Shotyk, W., 2012. Stibnite (Sb_2S_3) oxidative dissolution kinetics from pH 1 to 11. Geochim. Cosmochim. Acta 79, 127–139. https://doi.org/10.1016/j.gca.2011.11.033.

Boev, B., Jovanovski, G., Makreski, P., 2012. Geology and mineralogy of Allchar Sb-As-Tl-Au deposit. II. Congress of Geologists of Republic of Macedonia. Geol. Maced. 3, 215–232.

Bolanz, R.M., Bläß, U., Ackermann, S., Ciobota, V., Rösch, P., Tarcea, N., Popp, J., Majzlan, J., 2013. The effect of antimonate, arsenate and phosphate on the transformation of ferrihydrite to goethite, hematite, feroxyhyte, and tripuhyite. Clays Clay Miner 61, 11–25.

Burton, E.D., Hockmann, K., Karimian, N., 2020. Antimony Sorption to Goethite: Effects of Fe(II)-Catalyzed Recrystallization. ACS Earth Space Chem 4 (3), 476–487. https://doi.org/10.1021/acsearthspacechem.0c00013.

Cambel, B., Khun, M., 1983. Geochemical characteristics of black shales from ore-bearing complex of the Malé Karpaty. Geol. Carpath. 34, 15–44.

Chovan, M., Rojkovič, I., András, P., Hanas, P., 1992. Ore mineralization of the Malé Karpaty Mts. (Western Carpathians). Geol. Carpath. 43, 275–286.

Chovan, M., Háber, M., Jeleň, S., Rojkovič, I. (Eds.), 1994. Ore Textures in the Western Carpathians. Slovak Academic Press, pp. 1–219.

Cooper, R.G., Harrison, A.P., 2009. The exposure to and health effects of antimony. Indian J. Occup. Environ. Med. 13 (1), 3–10. https://doi.org/10.4103/0019-5278.50716.

Cutter, G.A., 1992. Kinetic controls on metalloid speciation in seawater. Mar. Chem. 40, 65–80.

Dauphas, N., John, S., Rouxel, O., 2017. Iron isotope systematics. Rev. Mineral. Geochem. 82, 415–510. https://doi.org/10.2138/rmg.2017.82.11.

Đorđević, T., Drahota, P., Kolitsch, U., Majzlan, J., Peřestá, M., Kiefer, S., Stöger-Pollach, M., Tepe, N., Hofmann, T., Mikuš, T., Tasev, G., Serafimovski, T., Boev, I., Boev, B., 2021a. Synergetic Tl and as retention in secondary minerals: an example of extreme arsenic and thallium pollution. J. Appl. Geochem. 135, 105114–105130. https://doi.org/10.1016/j.apgeochem.2021.105114.

Đorđević, T., Kolitsch, U., Drahota, P., Majzlan, J., Peřestá, M., Serafimovski, T., Tasev, G., Boev, I., Boev, B., 2021b. Tl Sequestration in the Middle Part of the Allchar Sb–As–Tl–Au deposit, North Macedonia. Goldschmidt Abstracts, 2021 Virtual Conference, Lyon, France, 4–9 July. 2021. https://doi.org/10.7185/gold2021.5196.

Fernandez, A., Borrok, D.M., 2009. Fractionation of Cu, Fe, and Zn isotopes during the oxidative weathering of sulfide-rich rocks. Chem. Geol. 264, 1–12. https://doi.org/10.1016/j.chemgeo.2009.01.024.

Ferrari, C., Méheut, M., Resongles, E., Freydier, R., Casiot, C., 2022. Equilibrium mass-dependent isotope fractionation of antimony between stibnite and Sb secondary minerals: a first-principles study. Chem. Geol. 611, 121115 https://doi.org/10.1016/j.chemgeo.2022.121115.

Ferrari, C., Resongles, E., Héry, M., Désoeuvre, A., Freydier, R., Delpoux, S., Bruneel, O., Casiot, C., 2023. Antimony isotopic fractionation during Sb(III) oxidation to Sb(V): Biotic and abiotic processes. Chem. Geol. 641, 121788 https://doi.org/10.1016/j.chemgeo.2023.121788.

Ferrari, C., Resongles, E., Freydier, R., Casiot, C., 2024. Antimony isotope fractionation during Sb(V) and Sb(III) adsorption on secondary Fe-minerals (schwertmannite, ferrihydrite) typical of mine waters. Appl. Geochem. 163, 105935 https://doi.org/10.1016/j.apgeochem.2024.105935.

Filella, M., Belzile, N., Chen, Y-W., 2002. Antimony in the environment: a review focused on natural waters: I. Occurrence. Earth-Sci. Rev. 57, 125–176. https://doi.org/10.1016/S0012-8252(01)00070-8.

Friedrich, A., Wildner, M., Tillmanns, E., Merz, P., 2000. Crystal chemistry of the new mineral brandholzite, $Mg(H_2O)_6[Sb(OH)_6]_2$, and of the synthetic analogues $M^{2+}(H_2O)_6[Sb(OH)_6]_2$ (M^{2+} = Mg, Co). Am. Mineral. 85, 593. https://doi.org/10.2138/am-2000-0422.

Grexová, A., 1991. Mineralogy of the Technological Products at the Sb Deposit Pezinok. Unpublished Diploma thesis. Comenius University, p. 66 (in Slovak).

Guillevic, F., Rossi, M., Resongles, E., Freydier, R., Ferrari, C., Quantin, C., Monvoisin, G., Poulenard, J., Arnaud, F., 2024. Multi-isotope (Pb, Sb) approach to trace metallic contaminant sources at a historical mining and metallurgical site. Chem. Geol. 649, 121958. https://doi.org/10.1016/j.chemgeo.2024.121958.

Guo, J., Su, L., Zhao, X., Xu, Z., Chen, G., 2016. Relationships between urinary antimony levels and both mortalities and prevalence of cancers and heart diseases in general US population, NHANES 1999–2010. Sci. Total Environ. 571, 452–460. https://doi.org/10.1016/j.scitotenv.2016.07.011.

He, M., Wang, N., Long, X., Zhang, C., Ma, C., Zhong, Q., Wang, A., Wang, Y., Pervaiz, A., Shan, J., 2019. Antimony speciation in the environment: Recent advances in understanding the biogeochemical processes and ecological effects. J. Environ. Sci. 75, 14–39. https://doi.org/10.1016/j.jes.2018.05.023.

Herath, I., Vithanage, M., Bundschuh, J., 2017. Antimony as a global dilemma: Geochemistry, mobility, fate and transport. Environ. Pollut. 223, 545–559. https://doi.org/10.1016/j.envpol.2017.01.057.

Horn, I., von Blanckenburg, F., 2007. Investigation on elemental and isotopic fractionation during 196 nm femtosecond laser ablation multiple collector inductively coupled plasma mass spectrometry. Spectrochim. Acta Part B 62, 410–422. https://doi.org/10.1016/j.sab.2007.03.034.

Horn, I., von Blanckenburg, F., Schoenberg, R., Steinhoefel, G., Markl, G., 2006. In situ iron isotope ratio determination using UV-femtosecond laser ablation with application to hydrothermal ore formation processes. Geochim. Cosmochim. Acta 70, 3677–3688. https://doi.org/10.1016/j.gca.2006.05.002.

Hu, X., He, M., Kong, L., 2015. Photopromoted oxidative dissolution of stibnite. Appl. Geochem. 61, 53–61.

Janković, S.R., 1993. Metallogenic features of the Alsar epithermal Sb–As–Tl–Au deposit (the Serbo-Macedonian metallogenic province). N. Jb. Mineral. (Abh.) 166, 25–41.

Janković, S.R., Jelenković, R., 1994. Thallium mineralization in the Allchar Sb-As-Tl-Au deposit. N. Jb. Mineral. (Abh.) 167, 283–297.

Jia, X., Kaufmann, A.B., Lazarov, M., Wen, B., Weyer, S., Zhou, J., Ma, L., Majzlan, J., 2024. Antimony isotope fractionation during kinetic Sb(III) oxidation by antimony-oxidizing bacteria Pseudomonas sp. J1. Environ. Sci. Technol. https://doi.org/10.1021/acs.est.3c10271.

Johnson, C., Beard, B., Weyer, S., 2020. Iron Geochemistry: An Isotopic Perspective, XII. Springer International Publishing. https://doi.org/10.1007/978-3-030-33828-2.

Kaufmann, A.B., Lazarov, M., Kiefer, S., Majzlan, J., Weyer, S., 2021. In situ determination of antimony isotope ratios in Sb minerals by femtosecond LA-MC-ICP-MS. J. Anal. At. Spectrom. 36, 1554–1567. https://doi.org/10.1039/D1JA00089F.

Kaufmann, A.B., Lazarov, M., Weyer, S., Števko, M., Kiefer, S., Majzlan, J., 2023. Changes in antimony isotopic composition as a tracer of hydrothermal fluid evolution at the Sb deposit Pezinok (Slovakia). Mineral. Deposita 1-17. https://doi.org/10.1007/s00126-023-01222-7.

Kiczka, M., Wiederhold, J.G., Frommer, J., Kraemer, S.M., Bourdon, B., Kretzschmar, R., 2010. Iron isotope fractionation during proton- and ligand-promoted dissolution of primary phyllosilicates. Geochim. Cosmochim. Acta 11, 3112–3128. https://doi.org/10.1016/j.gca.2010.02.018.

Kimball, B.E., Mathur, R., Dohnalkova, A.C., Wall, A.J., Runkel, R.L., Brantley, S.L., 2009. Copper isotope fractionation in acid mine drainage. Geochim. Cosmochim. Acta 73, 1247–1263. https://doi.org/10.1016/j.gca.2008.11.035.

Koděra, M., Andrusovová-Vlčeková, G., Belešová, O., Briatková, D., Dávidová, Š., Fejdiová, V., Hurai, V., Chovan, M., Nelišerová, E., Ženiš, P., 1986. Topografická mineralógia Slovenska. VEDA, Bratislava (in Slovak).

Lalinská-Voleková, B., Majzlan, J., Klimko, T., Chovan, M., Kučerová, G., Michňová, J., Hovorič, R., Göttlicher, J., Steininger, R., 2012. Mineralogy of weathering products

of Fe–As–Sb mine wastes and soils at several Sb deposits in Slovakia. Can. Mineral. 50, 481–500. https://doi.org/10.3749/canmin.50.1.000.
Lazarov, M., Horn, I., 2015. Matrix and energy effects during in-situ determination of Cu isotope ratios by ultraviolet-femtosecond laser ablation multicollector inductively coupled plasma mass spectrometry. Spectrochim. Acta B At. Spectrosc. 111, 64–73. https://doi.org/10.1016/j.sab.2015.06.013.
Leuz, A.-K., Johnson, C.A., 2005. Oxidation of Sb (III) to Sb (V) by O_2 and H_2O_2 in aqueous solutions. Geochim. Cosmochim. Acta 69, 1165–1172. https://doi.org/10.1016/j.gca.2004.08.019.
Leverett, P., Reynolds, J.K., Roper, A.J., Williams, P.A., 2012. Tripuhyite and schafarzikite: two of the ultimate sinks for antimony in the natural environment. Mineral. Mag. 76, 891–902. https://doi.org/10.1180/minmag.2012.076.4.06.
Li, L., Tu, H., Zhang, S., Wu, L., Wu, M., Tang, Y., Wu, P., 2019. Geochemical behaviors of antimony in mining-affected water environment (Southwest China). Environ Geochem Health 1–15. https://doi.org/10.1007/s10653-019-00285-8.
Liao, J., Tan, D., Qin, H., Liu, E., Chen, J., Ning, Z., Li, S., 2023. Antimony isotope fractionation and the key controls in the soil profiles of an antimony smelting area. J. Hazard. Mater. 454, 131553. https://doi.org/10.1016/j.jhazmat.2023.131553.
Lindsay, MB.J., Moncur, M.C., Bain, J.G., Jambor, J.L., Ptacek, C.J., Blowes, D.W., 2015. Geochemical and mineralogical aspects of sulfide mine tailings. Appl. Geochem. 57, 157–177. https://doi.org/10.1016/j.apgeochem.2015.01.009.
Liu, H., Sun, G., He, M., Feng, X., Lin, C., Ouyang, W., Liu, X., 2024. The composition and differences of antimony isotopic in sediments affected by the world's largest antimony deposit zone. Water Res. 254, 121427. https://doi.org/10.1016/j.watres.2024.121427.
Lobo, L., Devulder, V., Degryse, P., Vanhaecke, F., 2012. Investigation of natural isotopic variation of Sb in stibnite ores via multi-collector ICP-mass spectrometry – perspectives for Sb isotopic analysis of Roman glass. J. Anal. At. Spectrom. 27, 1304. https://doi.org/10.1039/c2ja30062a.
Loni, P.C., Wu, M., Wang, W., Wang, H., Ma, L., Liu, C., Song, Y., Tuovinen, O.H., 2020. Mechanism of microbial dissolution and oxidation of antimony in stibnite under ambient conditions. J. Hazard. Mater. 385, 121561 https://doi.org/10.1016/j.jhazmat.2019.121561.
Lottermoser, B.G., 2010. Mine Wastes (third edition): Characterization, treatment and environmental impacts. https://doi.org/10.1007/978-3-642-12419-8.
Luo, J., Xie, X., Shi, J., Wang, Y., 2023. Antimony isotope fractionation during adsorption on iron(oxyhydr)oxides. Environ. Sci. Technol. 58 (1), 695–703. https://doi.org/10.1021/acs.est.3c05867.
MacKinney, J.S., 2016. Antimony Isotopes as Indicators of Redox Reactions in Aqueous Systems: Fractionation during Sb (V) Reduction by Sulfide and Isotope Exchange Kinetics between Dissolved Sb (III) and Sb (V). Master thesis. Univ. Illinois.
Majzlan, J., 2021. Primary and secondary minerals of antimony. In: Filella, M., Gruyter, De (Eds.), Antimony, pp. 17–47.
Majzlan, J., Kiefer, S., Lilova, K., Subramani, T., Navrotsky, A., Dachs, E., Benisek, A., 2021. Chapmanite [Fe2Sb(Si2O5)O3(OH)]: thermodynamic properties and formation in low-temperature environments. Eur. J. Mineral. 33 (4), 357–371. https://doi.org/10.5194/ejm-33-357-2021.
Majzlan, J., Lalinská, B., Chovan, M., Bläß, U., Brecht, B., Göttlicher, J., Steininger, R., Hug, K., Ziegler, S., Gescher, J., 2011. A mineralogical, geochemical, and microbiological assessment of the antimony- and arsenic-rich neutral mine drainage tailings near Pezinok, Slovakia. Am. Mineral. 96, 1–13. https://doi.org/10.2138/am.2011.3556.
Majzlan, J., Števko, M., Lánczos, T., 2016. Soluble secondary minerals of antimony in Pezinok and Kremnica (Slovakia) and the question of mobility or immobility of antimony in mine waters. Environ. Chem. https://doi.org/10.1071/EN16013.
Maruška, M., Chovan, M., Ševc, J., 2000. Mineralogical and environmental evaluation of the settling poinds at the deposit Dúbrava in Nízke Tatry Mts. Slovak Geol. Magaz. 6, 61–69.
Masindi, V., Muedi, K.L., 2018. Environmental contamination by heavy metals. Heavy Metal 10, 115–132.
Mathur, R., Ruiz, J., Titley, S., Liermann, L., Buss, H., Brantley, S., 2005. Cu isotopic fractionation in the supergene environment with and without bacteria. Geochim. Cosmochim. Acta 69, 5233–5246. https://doi.org/10.1016/j.gca.2005.06.022.
Meija, J., Coplen, T.B., Berglund, M., Brand, W.A., de Bièvre, P., Gröning, M., Holden, N. E., Irrgeher, J., Loss, R.D., Walczyk, T., 2016. Isotopic compositions of the elements 2013 (IUPAC technical Report). Pure Appl, Chem 88, 293–306. https://doi.org/10.1515/pac-2015-0503.
Moynier, F., Vance, D., Fujii, T., Savage, P., 2017. The isotope geochemistry of zinc and copper. Rev. Mineral. Geochem. 82, 543–600. https://doi.org/10.2138/rmg.2017.82.13.
Okkenhaug, G., Zhu, Y-G., Luo, L., Lei, M., Li, X., Mulder, J., 2011. Distribution, speciation and availability of antimony (Sb) in soils and terrestrial plants from an active Sb mining area. Environ. Pollut. 159, 2427–2434. https://doi.org/10.1016/j.envpol.2011.06.028.
Parkhurst, D.L., Appelo, C.A.J., 1999. User's guide to PHREEQC (Version 2): A computer program for speciation, batch-reaction, one-dimensional transport, and inverse geochemical calculations, USGS/WRI-99-4259. US Geol. Surv, Denver, Colorado.
Pavićević, M.K., Cvetković, V., Amthauer, G., Bieniok, A., Boev, B., Brandstätter, F., Götzinger, M., Jelenković, R., Prelević, D., Prohaska, T., 2006. Quartz from Allchar as monitor for cosmogenic 26Al: Geochemical and petrogenetic constraints. Mineral. Petrol. 88, 527–550. https://doi.org/10.1007/s00710-006-0134-8.
Percival, T., Radtke, A.S., 1994. Sedimentary-rock-hosted dissemination gold mineralization in the Alšar district, Macedonia. Can. Mineral. 32, 649–655.
Polák, S., 1983. Chapmanite from Pezinok. Miner. Slov. 15, 565–566 (in Slovak).
Pršek, J., Lauko, Ľ., Valášková, M., 2009. Andorit VI z antimonitovej mineralizácie v Spišsko-gemerskom rudohorí (Zlatá Idka, Dobšiná-Tiefengründel. Mineralia Slovaca 41 (2), 183–190 (in Slovak).
Radková, A.B., Jamieson, H.E., Campbell, K.M., 2020. Antimony mobility during the early stages of stibnite weathering in tailings at the Beaver Brook Sb deposit, Newfoundland. Appl. Geochem. 115, 104528 https://doi.org/10.1016/j.apgeochem.2020.104528.
Resongles, E., Freydier, R., Casiot, C., Viers, J., Chmeleff, J., Elbaz-Poulichet, F., 2015. Antimony isotopic composition in river waters affected by ancient mining activity. Talanta 144, 851–861. https://doi.org/10.1016/j.talanta.2015.07.013.
Roper, A.J., Williams, P.A., Filella, M., 2012. Secondary antimony minerals: phases that control the dispersion of antimony in the supergene zone. Chem. Erde-Geochem. 72 (Suppl. 4), 9–14. https://doi.org/10.1016/j.chemer.2012.01.005.
Rouxel, O., Ludden, J., Fouquet, Y., 2003. Antimony isotope variations in natural systems and implications for their use as geochemical tracers. Chem. Geol. 200, 25–40. https://doi.org/10.1016/S0009-2541(03)00121-9.
Rudnick, R.L., 2018. Earth's Continental Crust. In: White, W.M. (Ed.), Encyclopedia of Geochemistry. Encyclopedia of Earth Sciences Series. Springer, Cham. https://doi.org/10.1007/978-3-319-39312-4_277.
Sejkora, J., Ozdín, D., Ďud'a, R., 2010. The supergene mineral association with brandholzie from Pernek, Malé Karpaty Mountains, Slovak Republic. J. Geosci. 55, 149. https://doi.org/10.3190/jgeosci.064.
Simate, G.S., Ndlovu, S., 2014. Acid mine drainage: Challenges and opportunities. J. Environ. Chem. Eng. 2 (3), 1785–1803. https://doi.org/10.1016/j.jece.2014.07.021.
Strmić, Palinkaš S., Hofstra, A.H., Percival, T.J., Borojević, Šuštarić S., Palinkaš, L., Bermanec, V., Pecskay, Z., 2018. Comparison of the Allchar Au-As-Sb-Tl deposit, Republic of Macedonia, with Carlin-type gold deposits. Rev. Econ. Geol. 20, 335–363. https://doi.org/10.5382/rev.20.10.
Tanimizu, M., Araki, Y., Asaoka, S., Takahashi, Y., 2011. Determination of natural isotopic variation in antimony using inductively coupled plasma mass spectrometry for an uncertainty estimation of the standard atomic weight of antimony. Geochem. J. 45, 27–32. https://doi.org/10.2343/geochemj.1.0088.
Tschan, M., Robinson, B.H., Schulin, R., 2009. Antimony in the soil–plant system–a review. Environ. Chem. 6, 106–115. https://doi.org/10.1071/EN08111.
Veldhuizen, H.J., MacKinney, J.S., Johnson, T.M., 2023. Kinetic fractionation of antimony isotopes during reduction by sulfide. ACS Earth Space Chem. 7 (12), 2603–2612. https://doi.org/10.1021/acsearthspacechem.3c00269.
Volkov, A.V., Serafimovski, T., Kochneva, N.T., Tomson, I.N., Tasev, G., 2006. The Alshar epithermal Au-As-Sb-Tl deposit, southern Macedonia. Geol. Ore Dep. 48, 175–192. https://doi.org/10.1134/S1075701506030020.
Wen, B., Zhou, J., Tang, P., Jia, X., Zhou, W., Huang, J., 2023. Antimony (Sb) isotopic signature in water systems from the world's largest Sb mine, Central China: Novel insights to trace Sb source and mobilization. J. Hazard. Mater. 446, 130622 https://doi.org/10.1016/j.jhazmat.2022.130622.
WHO, 2022. Guidelines for drinking-water quality: fourth edition incorporating the first and second addenda. World Health Organisation.
Wiederhold, J.G., 2015. Metal stable isotope signatures as tracers in environmental geochemistry. Environ Sci Technol. 49, 2606–2624. https://doi.org/10.1021/es504683e.
Wiederhold, J.G., Kraemer, S.M., Teutsch, N., Borer, P.M., Halliday, A.N., Kretzschmar, R., 2006. Iron isotope fractionation during proton-promoted, ligand-controlled, and reductive dissolution of goethite. Environ. Sci. Technol. 40, 3787–3793. https://doi.org/10.1021/es052228y.
Wilson, S.C., Lockwood, P.V., Ashley, P.M., Tighe, M., 2010. The Chemistry and Behaviour of Antimony in the Soil Environment with Comparisons to Arsenic: A Critical Review. Environ. Pollut. 158 (5), 1169–1181. https://doi.org/10.1016/j.envpol.2009.10.045.
Wilson, N., Webster-Brown, J., 2009. The fate of antimony in a major lowland river system, the Waikato River, New Zealand. Appl. Geochem. 24 (12), 2283–2292. https://doi.org/10.1016/j.apgeochem.2009.09.016.
Wu, Y., Sun, G., Huang, J.-H., Fan, H., Li, X., Zhou, M., Xia, Y., Feng, X., 2024. Antimony isotopic fractionation during intensice chemical weathering of basalt in the tropics. Geochim. Cosmochim. Acta 367, 29–40. https://doi.org/10.1016/j.gca.2023.12.029.
Zhai, D., Mathur, R., Liu, S.A., Liu, J., Godfrey, L., Wang, K., Vervoort, J., 2021. Antimony isotope fractionation in hydrothermal systems. Geochim. Cosmochim. Acta 12215. https://doi.org/10.1016/j.gca.2021.05.031.
Zhou, W., Zhou, A., Wen, B., Liu, P., Zhu, Z., Finfrock, Z., Zhou, J., 2022. Antimony isotope fractionation during adsorption on aluminum oxides. J. Hazard. Mater. 429, 128317 https://doi.org/10.1016/j.jhazmat.2022.128317.
Zhou, W., Zhou, J., Feng, X., Wen, B., Zhou, A., Liu, P., Sun, G., Zhou, Z., Liu, X., 2023. Antimony isotope fractionation revealed from EXAFS during adsorption on Fe (Oxyhydr)oxides. Environ. Sci. Technol. 57, 9353–9361. https://doi.org/10.1021/acs.est.3c01906.